Multiple sulfur isotope fractionation in hydrothermal systems in the presence of radical ions and molecular sulfur

Maria A. Kokh, Nelly Assayag, Stéphanie Mounic, Pierre Cartigny, Andrey Gurenko, Gleb S. Pokrovski

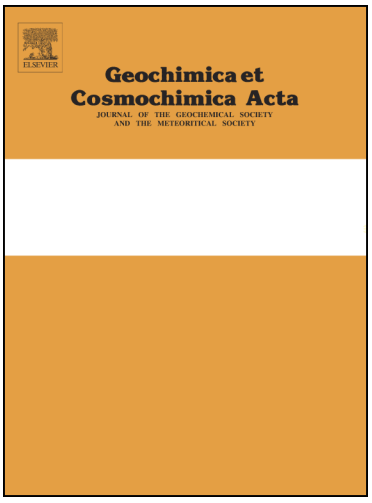

Multiple sulfur isotope fractionation in hydrothermal systems in the presence of radical ions and molecular sulfur

Maria A. Kokh, Nelly Assayag, Stephanie Mounic, Pierre Cartigny, Andrey Gurenko, Gleb S. Pokrovski

PII: S0016-7037(20)30376-8
DOI: https://doi.org/10.1016/j.gca.2020.06.016
Reference: GCA 11808

To appear in: *Geochimica et Cosmochimica Acta*

Received Date: 15 July 2019
Revised Date: 15 June 2020
Accepted Date: 19 June 2020

Please cite this article as: Kokh, M.A., Assayag, N., Mounic, S., Cartigny, P., Gurenko, A., Pokrovski, G.S., Multiple sulfur isotope fractionation in hydrothermal systems in the presence of radical ions and molecular sulfur, *Geochimica et Cosmochimica Acta* (2020), doi: https://doi.org/10.1016/j.gca.2020.06.016

Multiple sulfur isotope fractionation in hydrothermal systems in the presence of radical ions and molecular sulfur

Maria A. Kokh [1], Nelly Assayag [2], Stephanie Mounic [1], Pierre Cartigny [2], Andrey Gurenko [3], and Gleb S. Pokrovski [1]*

[1] Groupe Fluids at Extreme Conditions (FLEX), Géosciences Environnement Toulouse, GET, Université de Toulouse, CNRS, IRD, UPS, 14 avenue Edouard Belin, F-31400 Toulouse, France

[2] Université de Paris, Institut de Physique du Globe de Paris, CNRS, F-75005 Paris, France.

[3] Centre de Recherches Pétrographiques et Géochimiques (CRPG), 15 Rue Notre Dame des Pauvres, F-54500 Vandœuvre-lès-Nancy, France

* Corresponding author: Phone: (33)-(0)5-61-33-26-18; fax: (33)-(0)5-61-33-25-60; gleb.pokrovski@get.omp.eu

Revision 3

Geochimica et Cosmochimica Acta

15 June 2020

Keywords:
Trisulfur radical ion; disulfur radical ion, molecular sulfur; hydrothermal fluid; experiment; sulfur isotopes; mass dependent fractionation (MDF); mass independent fractionation (MIF).

Abstract:
This study is aimed to evaluate the role played by the sulfur radical ions ($S_3^{\bullet-}$ and $S_2^{\bullet-}$) and molecular sulfur (S^0) on sulfur isotope fractionation and to investigate if these species may leave an isotope fingerprint in hydrothermal systems. For this purpose, we combined i) experiments using a hydrothermal reactor with aqueous $S_3^{\bullet-}$($S_2^{\bullet-}$)-S^0-sulfate-sulfide fluids and pyrite across a wide range of temperatures (300-450°C), pressures (300-800 bar), fluid acidity (4<pH<8) and with elevated total sulfur concentrations (0.1-1.0 mol/kg fluid) favorable for formation of those polymeric sulfur species, ii) precise quadruple S isotope analyses of the different S-bearing aqueous species in sampled fluids and in-situ precipitated pyrite, and iii) thermodynamic modeling of sulfur aqueous speciation and solubility. Our results quantitatively confirm both equilibrium and kinetic SO_4-H_2S and pyrite-H_2S mass dependent fractionation (MDF) factors previously established using extensive experimental and natural data from more dilute fluids in which polymeric sulfur species are negligible. MDF signatures of S^0 measured in the sampled fluids of this study reveal different S^0-forming pathways such as i) breakdown on cooling of $S_3^{\bullet-}$ (and $S_2^{\bullet-}$) and other chain-like S^0 polymers only stable at high temperature and being isotopically identical to H_2S; ii) cyclooctasulfur (S_8^0, liquid or solid) precipitating by recombination of sulfate and sulfide and/or by exchange with polysulfide dianions (S_n^{2-}) on cooling and being slightly ^{34}S-enriched compared to H_2S (by ~2 ‰ of $\delta^{34}S$); and iii) a different type of S^0 resulting from thiosulfate irreversible breakdown and being highly ^{34}S-depleted (by ~12 ‰) relative to H_2S. Our data do not show any significant mass independent fractionation (MIF) of ^{33}S and ^{36}S, with $\Delta^{33}S$ and $\Delta^{36}S$ values of any S aqueous species and pyrite being within ±0.1 ‰ and ±1.0 ‰, respectively. Therefore, under the investigated experimental conditions, the radical $S_3^{\bullet-}$ ion is unlikely to generate significant MIF in the hydrothermal fluid phase and in pyrite and native sulfur precipitated therefrom. Our study supports the existing interpretations of small $\Delta^{33}S$ and $\Delta^{36}S$ variations between sulfide/sulfate-bearing fluid and pyrite as MDF in terms of reaction kinetics, different reaction pathways, and mass conservation effects such as mixing of S reservoirs or Rayleigh distillation. Our data extend, across a wider range of sulfur concentration and chemical speciation, the existing multiple S isotopes models that exploit such variations as a complement to the traditional $\delta^{34}S$ tracer to monitor the approach to equilibrium and evolution of hydrothermal fluids.

Highlights:

- Isotope signatures of sulfur species and pyrite have been studied in hydrothermal fluids.
- MDF equilibrium and kinetic SO_4-H_2S and pyrite-H_2S factors are quantified.
- No MIF anomalies are detected in the presence of sulfur radical ions.
- Isotope signature of molecular sulfur fingerprints the different mechanisms of S^0 formation.
- Several environments offer potential for MIF generation in fluid-mineral systems.

1. INTRODUCTION

Fractionation among the four stable isotopes of sulfur (^{32}S, ^{33}S, ^{34}S, and ^{36}S) has been used for tracing various geological processes since 1960's (e.g., Thode et al., 1961; Hulston and Thode, 1965). In most chemical and biological reactions, the sulfur isotope ratios obey mass-dependent fractionations (MDF); however, significant mass-independent fractionation (MIF) anomalies ($\Delta^{33}S$ >0.2‰)[1] were identified in pyrite and barite from Archean sedimentary rocks likely caused by SO_2 photolysis in the atmosphere (e.g., $\Delta^{33}S \approx$ -4 to +14 ‰; Farquhar et al., 2000; Johnston, 2011; Philippot et al., 2012), and also in sulfide minerals from a number of younger magmatic, hydrothermal and metamorphic rocks (e.g., Farquhar et al., 2002; Bekker et al., 2009; Thomassot et al., 2009; Cabral et al., 2013; Young et al., 2013; Delavault et al., 2016; Ripley and Li, 2017; LaFlamme et al., 2018a,b; Smit et al., 2019), which were interpreted as the reworking/recycling of Archean supracrustal rocks. These anomalies contrast with very small $\Delta^{33}S$ values, which are likely generated through MDF processes in low-temperature biological and inorganic sulfur redox reactions in solution or at the mineral surfaces (typically <0.15‰, Farquhar and Wing, 2003; Ono et al., 2006, 2007; Farquhar et al., 2007; Johnston, 2011). These MDF processes are quite well understood and result from mass-conservation effects (mostly mixing and Rayleigh distillation). Earlier theoretical work using quantum-chemistry modeling suggested that MIF could be generated by heterogeneous reactions (Lasaga et al., 2008), which was, however, not supported by a subsequent study (Balan et al., 2009).

In most hydrothermal fluids studied so far in nature (e.g., Kamyshny et al., 2014; Stefansson et al., 2015; McDermott et al., 2015) and laboratory (e.g., Ohmoto and Lasaga, 1982; Syverson et al., 2015; Meshoulam et al., 2016), relevant to active seafloor or surface geothermal systems and different shallow-crust hydrothermal deposits, sulfur isotope fractionation between the different inorganic sulfur species such as sulfate, sulfide, native sulfur, thiosulfate, and some organic thiol species has been interpreted by both equilibrium and kinetic MDF. This type of fractionation can only generate small deviations of ^{33}S isotope abundance from the classical MDF dependence ($\Delta^{33}S$ <0.05 ‰). In contrast, large $\Delta^{33}S$ anomalies (from -1.1 to +13.0‰) were reported in thermochemical sulfate reduction (TSR) reactions in hydrothermal experiments in the presence of amino-acids (Watanabe et al., 2009; Oduro et al., 2011). TSR phenomena were also invoked to explain the $\Delta^{33}S$ record in Paleoproterozoic black shales at Talvivarra, Finland (-0.6<$\Delta^{33}S$<1.3%, Young et al., 2013).

In the light of the large variety of sulfur isotope fractionation patterns exemplified above, detailed knowledge of sulfur chemical speciation in the fluid phase is required for understanding sulfur isotope

[1] Variations of S isotope ratios (normalized to the most abundant ^{32}S isotope) are conventionally expressed in the δ-notation relative to the V-CDT standard (Vienna-Cañon Diablo Troilite meteorite; Ding et al., 2001):
$\delta^{3x}S$ (in ‰) = $[(^{3x}S/^{32}S)_{sample}/(^{3x}S/^{32}S)_{V\text{-}CDT} - 1]\times 1000$, where x denotes 3, 4 or 6 for ^{33}S, ^{34}S, and ^{36}S, respectively.
MDF means that isotope ratios are proportional to the mass difference between isotopes yielding the relationships: $\delta^{33}S \approx (0.515\pm0.005)\times\delta^{34}S$, and $\delta^{36}S \approx (1.89\pm0.02)\times\delta^{34}S$ (e.g., Urey, 1947). MDF refers to isotope compositions deviating from this mass scaling law (i.e. $\Delta^{33}S \approx \delta^{33}S - 0.515\times\delta^{34}S$; see section 2.5 for details and rigorous equations).

fractionation, both MDF and MIF, in natural processes involving fluids. The major chemical forms of sulfur are known to be sulfate and sulfide (and sulfur dioxide and hydrogen sulfide in gas phase), which have been extensively studied over the last decades. However, recent discoveries of the sulfur radical ions $S_3^{\bullet-}$ and $S_2^{\bullet-}$ in geological fluids (Pokrovski and Dubrovinsky, 2011; Pokrovski and Dubessy, 2015) may lead to re-evaluate our vision of a number of geochemical processes in which sulfur is involved. For example, sulfur radicals enhance gold and platinum solubility in hydrothermal fluids involved in porphyry and orogenic deposit genesis (Pokrovski et al., 2015; 2019; Laskar et al., 2019). These radicals could also contribute to redox changes in the subcontinental lithospheric mantle by slab-liberated S-bearing fluids in subduction zones thereby affecting the sulfur release and metallogenic potential of the arc magmas (e.g., Rielli et al., 2017; Frimmel, 2018; Colin et al., 2020). At shallow-crust conditions, the $S_3^{\bullet-}$ ion was hypothesized to be a reaction intermediate controlling the kinetics of TSR processes and associated sulfur isotope fractionations (Truche et al., 2014; Pokrovski and Dubessy, 2015; Barré et al., 2017). The particular properties of $S_3^{\bullet-}$ make it different from the 'traditional' sulfur species and, therefore, might be responsible for MIF ^{33}S anomalies found in sulfides from hydrothermal settings and during TSR phenomena evoked above. This is because $S_3^{\bullet-}$ exhibits a magnetic moment due to a free electron, potentially enabling MIF, contrary to traditional sulfur molecules and ions (Buchachenko, 2001). Furthermore, $S_3^{\bullet-}$ is a structural and electronic analog of ozone (O_3) and its radicals exhibiting large ^{17}O MIF anomalies due to symmetry effects (e.g., $^{16}O^{16}O^{16}O$ vs $^{16}O^{17}O^{18}O$), which is a general quantum-level control potentially applicable to other triatomic molecules and radicals (Gao and Marcus, 2001; Babikov et al., 2003; Chakraborty et al., 2013; Reinhardt and Robert, 2013). The major challenge in studying $S_3^{\bullet-}$ and $S_2^{\bullet-}$ is that they are only stable and sufficiently abundant in aqueous solution at elevated temperatures and are not preserved on cooling/quench by very rapidly decomposing into traditional sulfur species such as sulfide, sulfur, polysulfides, and/or sulfate (Chivers and Elder, 2013; Pokrovski and Dubessy, 2015 and references therein).

Along with $S_3^{\bullet-}$ and $S_2^{\bullet-}$, another previously disregarded sulfur species in hydrothermal fluids, is a form of polymeric molecular sulfur (S_n^0, where n is undetermined number of uncharged S atoms in chain-like polymers), which has been identified by solubility and in-situ Raman spectroscopy measurements in S-rich solutions at >200°C (Dadze and Sorokin, 1993; Pokrovski and Dubessy, 2015; Barré et al., 2017), but its effect on both sulfur redox kinetics and isotope fractionation remains unexplored. This form of molecular sulfur is different from the previously recognized aqueous cyclo-octasulfur S_8^0 (e.g., Kamyshny, 2008; Pokrovski and Dubessy, 2015). Similarly to $S_3^{\bullet-}$, S_n^0 is not preserved on cooling in its original state, by transforming to native sulfur, molten or solid ($S_{(s,l)}$, composed of S_8 rings), which is a common low-temperature (<150°C) product of S-bearing fluids both in laboratory and natural hydrothermal-volcanic settings. Therefore, native sulfur may potentially record, through its isotope signature, processes of sulfur species transformation in fluids under elevated *T-P* conditions inaccessible to direct observation/sampling. Such processes include disproportionation of magmatic SO_2 (e.g., Kusakabe et al., 2000; Kouzmanov and Pokrovski, 2012), TSR reactions (Barré et al., 2017), or $S_3^{\bullet-}$ and S_n^0 transformations on cooling (e.g.,

Pokrovski and Dubessy, 2015). In this article, these different uncharged polymeric molecular sulfur forms are collectively termed as 'S^0'.

In an attempt to bring quantitative constraints on the role played by the trisulfur (and disulfur) radical ion and polymeric molecular sulfur on S isotope fractionation in hydrothermal environments, we combined *i)* experiments in $S_3^{\bullet-}$($S_2^{\bullet-}$)-S^0-sulfate-sulfide hydrothermal fluids, *ii)* precise analyses of the multiple sulfur isotope ratios in the different sulfur aqueous forms (sulfate, sulfide and S^0) and coexisting pyrite, and *iii)* thermodynamic modeling of sulfur aqueous speciation and solubility. The results contribute to better understanding of complex sulfur isotope fractionation processes in both ancient and modern hydrothermal systems relevant to various types of metal ore deposits formed by S-bearing fluids within the Earth's crust.

2. MATERIALS AND METHODS

2.1. Experimental strategy and conditions

Four experiments were conducted in synthetic aqueous sulfate-sulfide fluids from 300 to 450°C and from ~300 to ~700 bar to investigate both kinetic and equilibrium sulfur isotope fractionation over a wide range of $S_3^{\bullet-}$ concentrations (from <0.0001 to ~0.1 moles S per kg of fluid (m), Table 1). Aqueous thiosulfate solutions $K_2S_2O_3$ (-HCl-KOH) served as the source of sulfur, following the same approach as recent in-situ Raman spectroscopy studies that identified $S_3^{\bullet-}$, $S_2^{\bullet-}$ and S^0 (Pokrovski and Dubessy, 2015). Potassium was preferred to Na which forms at elevated temperatures a poorly soluble Na_2SO_4 solid compared to K_2SO_4 (Linke and Seidell, 1965). Thiosulfate breaks down in aqueous solution on heating above 150°C, producing dominantly sulfate and sulfide

$$S_2O_3^{2-} + H_2O = SO_4^{2-} + H_2S \quad (1)$$

Adding acid (HCl) or base (KOH) allows enhanced formation of protonated (HSO_4^-) or deprotonated (HS^-) species, respectively, enabling acidity buffering

$$SO_4^{2-} + H^+ = HSO_4^- \quad (2)$$

$$H_2S = HS^- + H^+ \quad (3)$$

Alternatively, acidity buffering at slightly acidic pH values may also be achieved by using alkali aluminosilicate mineral assemblages, such as quartz-muscovite-microcline, which was used in one of our experiments (m22, see below). Furthermore, equilibria between sulfate and sulfide at elevated temperatures impose oxygen fugacity (f_{O2}), which typically ranges, depending on pH, from HM-2 to HM+2 (where HM denotes the $\log f_{O_2}$ value of the conventional hematite-magnetite mineral buffer):

$$H_2S + 2\ O_2 = SO_4^{2-} + 2\ H^+ \quad (4)$$

The formation of $S_3^{\bullet-}$ in such sulfate-sulfide solutions can be formally described by the reaction

$$19\ H_2S + 5\ SO_4^{2-} + 2\ H^+ = 8\ S_3^{\bullet-} + 20\ H_2O \quad (5)$$

This reaction implies that the abundance of $S_3^{\bullet-}$ is controlled by total S concentration (S_{tot}, which is proportional to the sum of the dominant sulfate and sulfide), solution pH, and the H_2S/SO_4 ratio (and therefore

oxygen fugacity), with a maximum abundance at a given set of *T*, S_{tot} and pH at a H_2S/SO_4^{2-} ratio of 19/5. Note that this formal reaction in no way reflects the mechanisms of $S_3^{\bullet-}$ formation and breakdown, but only illustrates the fundamental thermodynamic controls on the $S_3^{\bullet-}$ equilibrium concentration in solution. In addition to the above S species produced by reactions (1) to (5), and depending on S and K total content, pH and *T-P* conditions, variable amounts of sulfate and sulfide ion pairs with K^+, SO_2, S_8^0 (both aqueous and molten), disulfur ion $S_2^{\bullet-}$, and polysulfide dianions S_n^{2-} will also form.

The concentrations of all these species can be estimated using available thermodynamic data (see section 2.6 and Table A2.1 for discussion and data sources). Figure 1 shows the calculated equilibrium distribution of the different sulfur species, using the best up-to-date thermodynamic data (but see section 2.6), in $K_2S_2O_3$ aqueous solutions over the *T-P*-S_{tot}-pH-redox range of this study, and Table 1 overviews the composition and different steps of the conducted experiments. In this manuscript, all pH values are thermodynamically calculated at the corresponding *T-P*-composition. Two exploratory runs (m22 and m29) at 350°C in acidic (pH ~4.5 at experimental *T-P*) and alkaline (pH ~7.3) solutions were designed to examine S isotope fractionation in a $S_3^{\bullet-}$-rich (~0.07 m S in the form of $S_3^{\bullet-}$) and $S_3^{\bullet-}$-poor (<0.001 m S) fluids, respectively. A more elaborated experiment (m32) consisted of two succeeding steps in slightly alkaline $S_3^{\bullet-}$ - poor conditions (~0.005 m S) at two contrasting temperatures, 300 and 450°C, followed by an acidification of the fluid at 450°C to increase $S_3^{\bullet-}$ concentration by a factor of 10 (~0.04 m S). In addition, the $S_2^{\bullet-}$ may also be present at such elevated temperatures (Fig. 1b; Pokrovski and Dubessy, 2015; Pokrovski et al., 2019). The last step of the three experiments above was conducted in the presence of pyrite (plus barite in m22) whose precipitation was induced by injecting, in-situ into the reactor, an $FeCl_2$ (plus $BaCl_2$ in m22) aqueous solution, thus simulating pyrite precipitation in natural hydrothermal fluids. Finally, a fourth experiment (m33) was conducted at 300°C at near-neutral pH (~5.3) by progressively diluting with water the initial $K_2S_2O_3$-bearing fluid leading to a decrease of $S_3^{\bullet-}$ concentration by a factor of 10 (from ~0.07 to 0.008 m S), to examine the effect of changing of $S_3^{\bullet-}$ abundance on sulfur isotope fractionation.

Our experimental systems offer a good analog for natural S-rich fluids in arc-related magmatic–hydrothermal systems hosting porphyry, skarn and epithermal Cu-Au-Mo deposits, which are characterized by typical temperatures of 250-500°C, pressures of 100-1000 bar, a wide pH (3-8) and redox (HM±2) ranges, typical salinities of 5-15 wt% of NaCl+KCl, the coexistence of sulfate and sulfide in a wide range of concentrations (from ~0.01 to a few wt% S), and the ubiquitous presence of pyrite (Einaudi et al., 2003; Kouzmanov and Pokrovski, 2012). Furthermore, the isotope fractionation patterns obtained in this study are also relevant to other hydrothermal settings and ore-deposit contexts that are all characterized by the presence of S-bearing fluids and iron sulfide minerals (e.g., seafloor geothermal systems, orogenic and sedimentary basin metal deposits).

2.2. Experimental setup

The runs were conducted using a Coretest reactor (Fig. 2) equipped with a flexible gold inner cell with a Ti 2-μm frit filter in its head, i.e. analogous to Seyfried et al. (1987) and Rosenbauer et al. (1993) and recently adapted to multicomponent and S-rich systems as described previously (Pokrovski et al., 2015; Kokh et al., 2017). The gold cell (120-180 cm^3 of initial volume) is inserted into a high-pressure vessel (~1000 cm^3 volume, type 316 SS, stainless steel), which is filled with water as a pressure medium controlled by a gas-driven pump, and placed into an electrically heated (±1°C) rocking furnace. An ultrafast sampling device, analogous to that of Seewald and Seyfried (1990), consists of a titanium tube attached to two high-pressure titanium valves and a rigid titanium vial (~2.5 cm^3) tightly assembled to the second valve. The device enables an almost instantaneous (<1 s) transfer into the vial of a portion of the fluid phase pushed by the internal pressure from the reactor. This design prevents sulfur precipitation or degassing (see Kokh et al., 2017 for details), which would have inevitably occurred in S-bearing systems using traditional sampling procedures. Prior to experiments, the gold cell was cleaned with HNO_3 and annealed at 380°C for 1 h to allow for a greater malleability and deformation.

During an experiment, fluids were periodically sampled and processed as described in sections 2.3 and 2.4. In the course of experiments m32 and m33, aqueous HCl or pure water were injected into the cell, initially loaded with a thiosulfate solution, using a calibrated capstan pump (total volume = 12 cm^3). This injection allows controlled changes of the fluid pH and S_{tot} concentration and, consequently, the sulfur speciation (in particular, the amount of S^0 and $S_3^{\bullet-}$, see Table 1 and Fig. 1). Precipitation of pyrite (together with barite in m22), in the final stage of three experiments (m22, m29 and m32), was induced by injection into the reactor of an $FeCl_2$ (-$BaCl_2$) aqueous solution in amounts not exceeding those of aqueous sulfide. Then the fluid composition continued to be monitored by periodic sampling, and the solid was finally recovered upon complete cooling of the reactor.

2.3. Chemical analyses of sampled fluids

Because the complex sulfur speciation at elevated *T-P* strongly evolves upon fluid cooling (Fig. 1d), the original species identity and distribution cannot be adequately recovered in quenched samples. Therefore, special procedures are required for separation and preservation of the different sulfur forms for chemical and isotope analyses. These procedures are based on improved methods developed in our previous studies of S-rich fluid systems (e.g., Pokrovski et al., 2008; Kokh et al., 2016). Each sampling session comprised multiple samples of the fluid phase (usually 5, amounting 0.5 to 1.0 g each), directly taken into specific aqueous reagents (concentrated solutions of I_2, $Cd(CH_3COO)_2$, $Zn(CH_3COO)_2$, NH_3) placed in the sampling vial to allow for quantitative recovery and preservation of the different forms of sulfur, as well as dissolved chloride, potassium, iron and gold (Table A1.1). Total aqueous sulfur (S_{tot}) was analyzed in samples taken into aqueous ammonia (28 wt% NH_3) by inductively coupled plasma - atomic emission spectrometry (ICP-AES) and high-performance liquid chromatography (HPLC) after complete oxidation by hydrogen peroxide (30 wt% aqueous H_2O_2) of all S forms to sulfate. Total aqueous chloride was also analyzed by HPLC in the same NH_3

and H_2O_2-treated samples. Total reduced sulfur (S_{red}, comprising H_2S/HS^-/KHS, S_n^{2-} and, eventually, SO_2 and unreacted thiosulfate) was trapped in HCl aqueous solution containing an excess of iodine over sampled sulfur, and quantified by titration of the remaining I_2 by a standard thiosulfate solution, since all these reduced S species react with I_2 (e.g., Charlot, 1966; Dadze and Sorokin, 1993). Sulfide-type sulfur ($S_{sulfide}$, comprising H_2S, HS^- and KHS) was separated from the other sulfur forms by sampling the fluid into a cadmium acetate solution of near-neutral pH (~6), which results in quantitative precipitation of all sulfide species as poorly soluble Cd sulfide (CdS solubility is <µmol Cd/kg fluid), followed by iodometric titration in an I_2-HCl solution. Oxygen gas in the air space of the vial before sampling is less than 0.001 mmol/L, compared to 10s to 100s mmol/L of potentially oxidizable S species in the fluid (e.g., H_2S), so that oxidation by air is negligible. Sulfate-type aqueous sulfur ($S_{sulfate}$, comprising SO_4^{2-}, HSO_4^-, and their K^+ ion pairs, existing at experimental *T-P* conditions, Fig. 1) was quantified by HPLC as the SO_4^{2-} ion in water-diluted near-neutral pH acetate solutions, after removal of sulfide as CdS precipitate by centrifugation. The presence of thiosulfate in the supernatant was also checked by HPLC, but could not be quantified.

Molecular sulfur was separated from other S species as hexane extracts (hereafter S^0_{hexane}) collected from samples trapped into Cd acetate solution followed by removal of CdS via centrifugation. The hexane fraction was then analyzed for S^0 by UV spectrometry at a wavelength of 264 nm calibrated using reference solutions prepared by dissolving a given amount of native sulfur in hexane. The analytical uncertainty on the S^0 concentration determination in our systems is typically ±50%, mostly because impurities common in our chemically complex samples (including acetate and its decomposition products that may partition into hexane) absorb in the same UV range. All vials and tubes were also rinsed with hexane after recovery of each sampled solution, and analyzed for S^0, which has always been found below the detection limit (<0.0001 m S). An independent way for estimating S^0 concentrations in the sampled fluid was using sulfur mass balance between S_{tot} and the sum of sulfate and reduced sulfur (hereafter $S^0_{balance}$), because S^0 does not react with iodine and does not precipitate with Cd or Ba acetate.

Concentrations of potassium, gold and iron were determined by ICP-AES and, selectively, by flame atomic absorption spectrometry (FAAS), after the NH_3 sample treatment with aqua regia. This treatment consists of i) gentle evaporation of the sample on hot plate (60-80°C) in a cleaned Teflon vial (Savilex ®), ii) reaction of the residue with 2 g of hot aqua regia in the closed vial (at 120°C for 2h), followed by iii) gentle evaporation of solution (at 60-70°C) to 0.2-0.3 g, and iv) dilution of the remaining solution by ultra-pure 0.5 wt% HCl - 1.5wt% HNO_3 in water. More details on the chemical procedures and associated uncertainties are given in Kokh et al. (2016, 2017). The results of fluid analyses are reported in Table 2 and shown as a function of run duration in Fig. 3.

2.4. Processing of sampled fluids for sulfur isotope analyses

The sulfur isotope ratios were analyzed (depending on the experiment) in the initial thiosulfate and sampled aqueous sulfate, sulfide and molecular sulfur (if available), and in the precipitated pyrite recovered

after the run. Like for the chemical analyses described above, the challenge was to accurately separate the different sulfur forms on sampling to avoid, as much as possible, both chemical recombination and isotope exchange/mixing among these forms in our S-rich systems on cooling. The fluid sample treatment is described as follows and summarized in Table A1.1.

In an exploratory experiment (m22), sulfur samples were taken into an aqueous solution of zinc and barium acetate, resulting in simultaneous precipitation of ZnS and $BaSO_4$ in the sampling vial. However, difficulties were encountered when converting ZnS to H_2S from the fine-grained ZnS-$BaSO_4$ mixture that prevented ZnS, being armored by $BaSO_4$, to quantitatively react with the HCl solution, resulting in low yields. Consequently, the experimental protocol was changed in the subsequent experiments. In runs m29, m32, and m33, aqueous sulfide was trapped as ZnS by placing 1.0-1.5 mL of 1 m zinc acetate solution into the sampling vial. The formed ZnS precipitate was centrifuged (3800 rpm for 15 min) to separate it from the solution, washed with deionized water and dried at 90°C for subsequent isotope analyses. After centrifugation, the supernatant solution was reacted with 1.5 mL of 1 m barium acetate to precipitate $BaSO_4$, which was then centrifuged, washed, dried similarly to the ZnS precipitate, and reserved for isotope analyses.

Molecular sulfur S^0 was separated by extraction into hexane after precipitating H_2S as CdS when sampling the fluid directly into a 1 mL of 1 m cadmium acetate solution. This procedure prevents *i)* isotope exchange between S^0 and H_2S/HS^- prone to rapid re-equilibration, and *ii)* possible recombination of sulfate and sulfide to form additional S^0. Despite all these precautions, native sulfur might still partly precipitate, especially in S-rich acidic solutions, during the fluid passage through the sampling tubes and valves before reaching the vial with the trapping reagent, and thus get transferred into the vial together with the fluid. Although the different origins and formation mechanisms of S^0 in the sampled fluid cannot be distinguished by bulk S^0 chemical analyses, their isotopic composition is expected to reflect those mechanisms. The supernatant containing sulfate and S^0 was separated from the CdS precipitate by centrifugation (3800 rpm for 15 min), filtered (0.45 μm) and placed into a glass flask with 30 mL of hexane and 10 mL of glycerol (the latter was used to protect the eventually remaining thiosulfate from oxidation that might lead to additional formation of molecular sulfur; Dadze and Sorokin, 1993). The aqueous solution and the hexane phase were allowed to react for at least 48 h to enable the complete extraction of S^0 into the hexane phase, as checked by time-dependent analyses. The S^0-bearing hexane fraction was then recovered and analyzed for S^0 by UV-Vis spectrometry (section 2.3). After the UV analysis, the hexane was gently evaporated at 50°C and the precipitated sulfur was saved for isotope analyses.

The sulfur isotope composition of the initial thiosulfate was measured separately in its sulfane (S^{2-}) and sulfonate (S^{6+}) parts according to the slightly modified protocols of Uyama et al. (1985) and Syverson et al. (2015). An aqueous 0.1 m $AgNO_3$ solution was used to precipitate the sulfane sulfur as Ag_2S from an aqueous 0.05 m $K_2S_2O_3$ solution. The supernatant was separated from the precipitate by centrifugation and reacted with an excess of barium acetate to precipitate the sulfonate part as $BaSO_4$, which was then recovered after centrifugation.

2.5. Quadruple sulfur isotope analyses and isotope standardization and notation

Measurements of the four stable sulfur isotope ratios were realized with a gas source Ion Ratio Mass Spectrometer (IRMS) Thermo Finnigan MAT 253 at the Institut de Physique du Globe de Paris (IPGP) as described by Labidi et al. (2012). Samples of ZnS, $BaSO_4$ and S^0 were converted to solid silver sulfide (Ag_2S) using established techniques (Thode et al., 1961; Canfield et al., 1986; Labidi et al., 2012). The obtained Ag_2S was in turn quantitatively converted to sulfur hexafluoride gas (SF_6) purified cryogenically by distillation and by gas chromatography before being introduced into the spectrometer (Appendix A1 for details). Procedural blanks, associated with sulfur conversion into Ag_2S and subsequent Ag_2S fluorination and purification, are too low to be quantified (nano-molal levels). The S isotope composition of SF_6(g) was analyzed at mass-to-charge ratio values of 127, 128, 129, and 131 corresponding to the $S^{32}F_5^+$, $S^{33}F_5^+$, $S^{34}F_5^+$, and $S^{36}F_5^+$ ions, respectively (note that fluorine has a single stable isotope, ^{19}F, which avoids any mass interference). Typical analytical errors of our measurements in a single session (2 standard deviations, 2 SD) are 0.05 ‰, 0.01 ‰, and 0.18 ‰ for $\delta^{34}S$, $\Delta^{33}S$ and $\Delta^{36}S$, respectively. Typical external reproducibility on $\delta^{34}S$, $\Delta^{33}S$, and $\Delta^{36}S$ among different sessions (conducted over >1 year and by several analysts) and parallel chemical treatments of the same sampled fluid are 0.6 ‰, 0.02 ‰, and 0.35 ‰ (2 SD), respectively, as estimated by four independent measurements of the pyrite sample from experiment m29.

All $\delta^{34}S$, $\Delta^{33}S$ and $\Delta^{36}S$ data obtained in this study are reported relative to the V-CDT standard, which is a virtual S isotope reference adopted instead of the previously used natural Cañon Diablo Troilite (CDT) meteorite, that was found to be slightly isotopically heterogeneous (Ding et al., 2001). The V-CDT standard was defined on the base of a homogeneous synthetic standard, IAEA-S-1 (Ag_2S), with a $\delta^{34}S$ value of -0.30‰ relative to V-CDT (Ding et al., 2001; references therein). Because there is presently no international standard for $\delta^{33}S$ and $\delta^{36}S$, in this study we anchored our ^{33}S and ^{36}S data to the V-CDT reference scale, for consistency with the recent studies (Ono et al., 2007) assuming that $\delta^{33}S_{V\text{-}CDT} = -0.055\pm0.14$ ‰, $\delta^{36}S_{V\text{-}CDT} = -1.37\pm0.5$ ‰, $\Delta^{33}S_{V\text{-}CDT} = 0.100\pm0.003$ ‰, and $\Delta^{36}S_{V\text{-}CDT} = -0.8\pm0.1$ ‰ (see also Geng et al., 2019 for a recent inter-comparison). Note that this normalization has no consequences on calculations of isotope fractionation factors between different sulfur species. Values of $\Delta^{33}S$ and $\Delta^{36}S$ were calculated according to Farquhar and Wing (2003):

$$\Delta^{33}S_{V\text{-}CDT} = \delta^{33}S_{V\text{-}CDT} - 1000 \times [(1 + \delta^{34}S_{V\text{-}CDT}/1000)^{\lambda_{33}} - 1)] \quad (6)$$

$$\Delta^{36}S_{V\text{-}CDT} = \delta^{36}S_{V\text{-}CDT} - 1000 \times [(1 + \delta^{34}S_{V\text{-}CDT}/1000)^{\lambda_{36}} - 1)] \quad (7)$$

where $\lambda 33$ and $\lambda 36$ are adopted as 0.515 and 1.889, respectively (note that these values may vary by a few ‰ in different equilibrium and kinetic isotope exchange reactions, Young et al., 2012). Isotope fractionation between the different sulfur forms (here given for $\delta^{34}S$) is expressed relative to aqueous sulfide analyzed as ZnS:

$$1000\times\ln\alpha_i \approx \delta^{34}S_i - \delta^{34}S_{sulfide} \quad (8)$$

where *i* denotes sulfate sulfur (collectively termed as SO_4), molecular sulfur (S^0) or pyrite (Py), and α_i is the conventional isotope fractionation factor between *i*-species and sulfide, $(^{34}S/^{32}S)_i/(^{34}S/^{32}S)_{sulfide}$. The results of S isotope analyses obtained in this study are reported in Tables 3 and 4 and plotted in Figs 5 to 8.

2.6. Chemical equilibrium calculations of aqueous sulfur speciation and solubility

Sulfur speciation and solubility in the fluid phase of the experimental systems were modelled using available thermodynamic data, and the results were compared with the measured S species concentrations. Calculations were performed using the HCh software package and associated Unitherm database, allowing chemical equilibrium simulations in fluid-mineral systems (Shvarov, 2008; 2015), and accounting for non-ideality of the fluid using the extended Debye-Hückel equation (Helgeson et al., 1981). The selection of thermodynamic data sources was discussed in detail elsewhere (Pokrovski et al., 2015, 2019; Kokh et al., 2017), and will be only briefly summarized here.

The thermodynamic properties of the minerals, major fluid components, and most aqueous ionic sulfur species were taken from the updated SUPCRT (Johnson et al., 1992), JANAF (Chase, 1998), and USGS (Robie and Hemingway, 1995) databases, complemented by recent data for ionic sulfur forms including $S_3^{\bullet-}$ (Pokrovski and Dubessy, 2015; references therein) using the revised and extended HKF (Helgeson-Kirkham-Flowers) equation of state (Oelkers et al., 2009; Sverjensky et al., 2014; references therein). The thermodynamic properties of the aqueous 'gas-like' sulfur nonelectrolytes, H_2S, SO_2, as well as H_2 and O_2, were adopted from Akinfiev and Diamond (2003) whose model provides a more accurate description of such species over the *T-P* range relevant to our study (300-450°C; <1 kbar) than the SUPCRT database, which was based on a more limited experimental dataset for derivation of the HKF model coefficients for those species. The thermodynamic properties of the polysulfide ions (S_n^{2-}, where *n* is between 2 and 6) and aqueous S_8^0 at 300-450°C were taken from Pokrovski and Dubessy (2015); both types of species were found to be negligible in the fluid at the elevated temperatures of our experiments (<0.001 m S; Fig. 1). The $S_2^{\bullet-}$ radical ion, with a stability constant at 450°C and 700 bar from Pokrovski et al. (2019), was predicted to account for ~0.01 m S in experiment m32, which is comparable to $S_3^{\bullet-}$ (Fig. 1b). However, the uncertainties on such predictions are large (of an order of magnitude); furthermore, the $S_2^{\bullet-}$ ion is expected to be negligible in our lower-*T* experiments since it has not been detected by Raman resonance spectroscopy below 450°C (Pokrovski and Dubessy, 2015). The sources of thermodynamic properties of solid phases and aqueous species used in the modeling are summarized in Table A2.1 and the results of calculations for typical conditions of our experiments are shown in Fig. 1.

The missing species in these calculations are molecular sulfur polymers S_n^0 forming around 300°C as detected by in-situ Raman spectroscopy (Pokrovski et Dubessy, 2015; Barré et al., 2017) and protonated polysulfides (HS_n^-), for which no thermodynamic data are currently available at elevated temperatures. Estimations of Pokrovski and Dubessy (2015) suggest that S_n^0 equilibrium concentrations in thiosulfate solutions more concentrated than those of our study (S_{tot} ~2 m), attain maximum values of the order of 0.1-

0.2 m S around 300°C, and show sharply decreasing amounts with increasing *T* and/or decreasing S_{tot} concentration. However, considering the large errors of such estimates and possible multiple and likely out-of-equilibrium origins of molecular sulfur found in the experiments of this study, quantification of S^0 equilibrium concentrations cannot confidently be made at present. Similarly, the amount of HS_n^- cannot be quantitatively assessed, but the absence of H-S vibrations in the Raman spectra of Pokrovski and Dubessy (2015) and Barré et al. (2017) strongly suggests that their concentrations at *T-P*-pH conditions of our experiments are likely to be too small to affect sulfur mass and isotope balance.

New data obtained in the course of this study allowed estimations of the amount and origin of S^0 at elevated temperatures based of S^0 isotope signatures, and a revision of the stability of the major sulfate-bearing species, KSO_4^- (Fig. 1) based on the observation of K_2SO_4(s) precipitation in one experiment at 450°C (m32; section 4.1.1 and Appendix A3). The revised calculations, with corrected KSO_4^- stability constants, of equilibrium aqueous sulfate and sulfide concentrations for each experimental step will be compared with their experimental counterparts (Fig. 4) and help to better constrain the interpretation of the S isotope patterns.

3. RESULTS

3.1. Sulfur chemical speciation in the fluid phase

3.1.1. Experiments at 350°C (m22, m29)

Two experiments have been conducted at 350°C and 300-400 bar in acidic (0.5 m $K_2S_2O_3$-0.14 m HCl, $pH_{350°C}$ ~4.5, run m22) and less concentrated slightly alkaline (0.2 m $K_2S_2O_3$-0.09 m KOH, $pH_{350°C}$ ~7.3, run m29) solutions, corresponding to $S_3^{\bullet-}$-rich (~0.07 m S) and $S_3^{\bullet-}$-poor (~0.002 m S) compositions, respectively. The concentrations of S species measured in these experiments are reported in Table 2 and their evolution with time is shown in Fig. 3a,b. In both experiments, before $FeCl_2$ injection, sulfate and sulfide represent the major fraction of dissolved sulfur. Reduced sulfur (S_{red}) is slightly higher than sulfide, by 0.01 to 0.04 m S, in the acidic experiment (m22); the difference might be due to the presence of minor quantities of SO_2 which is titrated by iodine together with sulfide. Reduced sulfur concentrations in the alkaline experiment (m29) are identical to those of sulfide. There are no discernable changes of the species concentration with time, suggesting that a chemical steady state is reached at this temperature within less than a few days. Total S concentrations (S_{tot}) analyzed in the less concentrated alkaline-pH run (m29) match the sum of $S_{sulfate}$ and S_{red} concentrations, implying an insignificant contribution of other S species that might have been omitted by our analytical protocols (<0.03 m S). In contrast, significant imbalance (up to 0.3 m S) between S_{tot} and the sum of S_{red} and $S_{sulfate}$ is apparent in the more concentrated acidic run (m22). This imbalance ($S^0_{balance}$) is attributed to the presence of molecular sulfur S^0 in the sampled fluid, which can react neither with iodine nor with cadmium or barium acetate. This $S^0_{balance}$ may have multiple origins that will be

discussed in section 4. In the next step of both experiments, after the injection of $FeCl_2$ (m29) and KCl-$FeCl_2$-$BaCl_2$ (in m22), S_{tot} becomes largely dominated by sulfate given that a major part of reduced sulfur precipitated as pyrite. Concentrations of S_{tot} are similar within errors to $S_{sulfate}$ in m29, and are slightly higher than $S_{sulfate}$ in m22, likely due to the presence of minor amounts of SO_2 favored by acidic pH (Fig. 1).

3.1.2. Experiment at 300 and 450°C (m32)

More complete information about sulfur speciation has been gained in a subsequent experiment conducted at 300 and 450°C (m32), with the development of a protocol for molecular sulfur analysis (see section 2.3). This experiment was started in alkaline solution (0.5 m $K_2S_2O_3$-0.3 m KOH $pH_{300°C}$ ~7) at 300°C, 500 bar and run for 13 days (step m32/1); then the temperature was raised to 450°C and kept for 14 days ($pH_{450°C}$ ~8, m32/2). In a next step lasting 8 days (m32/3), an HCl solution was injected into the reactor resulting in acidification ($pH_{450°C}$ ~7), allowing a better identification of $S_3^{\bullet-}$ whose abundance is predicted to increase at more acidic pH (Table 1, Fig. 1). In the final step (m32/4, lasting 8 days), a $FeCl_2$ solution was injected, resulting in pyrite precipitation and further fluid acidification ($pH_{450°C}$ ~6). Total K and S concentrations steadily decrease at a molar K/S ratio close to 2 with time during the 300°C step (Fig. 3c and A3.1). This decrease suggests the precipitation of K_2SO_4(s), which is known to have a retrograde solubility with temperature (Pokrovski and Dubessy, 2015). Further decrease of S and K concentrations is observed as the temperature was raised to 450°C, following by stabilization for ~1 week, suggesting an attainment of steady state concentrations. The retrograde solubility of K_2SO_4(s) was apparent at the 450°C stage during a temporary heating regulation problem before sample #6 (Table 2, Fig. 3c), causing the temperature to decrease to ~260°C, and before sample #7, causing the temperature to increase to ~460°C. The solubility of K_2SO_4(s) rapidly responded to these temperature changes by increasing above and then decreasing below the steady-state values obtained in 2 previous samples #4 and #5 (Table 2; Fig. 3c, A3.1).

During the 300°C stage (m32/1), measured concentrations of sulfate and sulfide remained constant over ~1 week, but their sum was inferior to that of S_{tot} by a factor of ~2 (Table 2, Fig. 3c), demonstrating the presence of analytically unreactive molecular sulfur ($S^0_{balance}$). Concentrations of $S^0_{balance}$ decreased by ~50% accompanied by an increase in both sulfate and sulfide (in the 2nd week), reflecting a slow and complex kinetics of thiosulfate transformation. A fourth species contributing to aqueous S is the thiosulfate ion, $S_2O_3^{2-}$, which was detected by HPLC analyses in sample #1 solution after separation of ZnS. The presence of undecomposed $S_2O_3^{2-}$ and/or its possible intermediate decomposition products (SO_3^{2-}) at this stage is also independently confirmed by the systematically higher measured concentrations of S_{red} compared to $S_{sulfide}$, since both thiosulfate and sulfite are titratable by iodine, but do not precipitate with Cd or Zn.

The *T* rise to 450°C after that step resulted in a drop of $S^0_{balance}$ concentrations by a factor of 5 to 10 as compared to the preceding sampling at 300°C (Fig. 3c). It should be noted that the S^0 values exhibit a large scatter due to both analytical difficulties for measuring S^0 in hexane extracts (S^0_{hexane}) and the use of mass-balance relations ($S^0_{balance}$) for deriving close-to-zero values (~0.01 m S). Yet, despite the scatter, the S^0_{hexane} concentrations appear, on average, quite similar to the $S^0_{balance}$ ones (Fig. A4.3), yielding a mean value of

0.04±0.02 m S (1 SD) for S^0 concentration for the whole set of datapoints over the three steps at 450°C (m32/2, 3, 4). Both types of S^0 data do not show any clear tendency as a function of elapsed time (Fig. 3c).

3.1.3. Experiment at 300°C and near-neutral pH (m33)

A fourth experiment was conducted at 300°C and 500 bar in 0.5 to 0.2 m $K_2S_2O_3$ solution at near-neutral pH ($pH_{300°C}$ ~5.3). This experiment was designed to better explore the effect of dilution resulting in large changes in $S_3^{\bullet-}$ (and S^0) concentrations without much changing the overall solution chemistry and acidity. At the initial stage (~0.5 m $K_2S_2O_3$, m33/1), sulfate and sulfide account for >60% of S_{tot} (Table 2). There are no systematic changes within errors of their concentrations with time, suggesting that a chemical steady state is reached. Likewise, there is no systematic difference between measured S_{red} and $S_{sulfide}$ concentrations, suggesting the absence of significant amounts (>0.02 m S) of reduced species other than H_2S/HS^- (e.g., polysulfide ions, SO_2, or undecomposed thiosulfate). In contrast, there is yet significant imbalance (up to 30% S_{tot}) between S_{tot} and the sum of $S_{sulfide}$ and $S_{sulfate}$, due to the presence of molecular sulfur ($S^0_{balance}$, Table 2), as was also confirmed by direct analyses of S^0_{hexane}. After the first injection of water, this imbalance is significantly reduced as a result of dilution (to ~15% S_{tot}). After the second injection of water, the S^0 fraction further decreased to become <5% S_{tot} after 1 week (Table 2, Fig. 3d). Like in experiment m32, both types of S^0 datapoints (S_{hexane} and $S_{balance}$) are quite scattered, but without any systematic trends between them (Fig. A4.3).

3.2. Sulfur isotope ratios in the fluid phase and pyrite

In two exploratory experiments (m22 and m29), only a limited dataset could be obtained on S isotope ratios of the different species (Table 3, Fig. A4.1 and A4.2). Most isotope data have been obtained on $S_{sulfide}$ (trapped as ZnS) and S^0 (analyzed by the CRS treatment of the ZnS-$BaSO_4$ mixture in m22; Appendix A1). Only few data points could be collected from $S_{sulfate}$ (trapped as $BaSO_4$) due to imperfections in separating ZnS from $BaSO_4$. The $\delta^{34}S_{sulfide}$ and $\delta^{34}S_{S^0}$ values are consistently more negative, by 14-21 ‰, than the $\delta^{34}S_{sulfate}$ values; however, the paucity of the $BaSO_4$ data does not allow the identification of any systematic trends with time.

A more extensive sulfur isotope data set has been obtained in experiment m32 (Table 3, Fig. 5a and 6). The isotope composition of sulfonate (O_3-S-) and sulfane (-S) sulfur of the initial thiosulfate (which decompose respectively to sulfate and sulfide according to reaction 1), evolves upon heating to 300°C, with sulfate and sulfide becoming through time ^{34}S-enriched and ^{34}S-depleted, respectively. In other words, the difference in $1000\times\ln\alpha_{SO4}$ ($\delta^{34}S_{sulfate} - \delta^{34}S_{sulfide}$) at each given moment increases with time, yet without reaching a steady state at 300°C (Fig. 5c). This evolution is mainly controlled by the increase in $\delta^{34}S_{sulfate}$, whereas $\delta^{34}S_{sulfide}$ remains constant within errors (Fig. 5a); this clearly indicates that at least a third S isotope pool is being formed. After the temperature rise to 450°C, $\delta^{34}S_{sulfide}$ values stay constant while $\delta^{34}S_{sulfate}$ values

increase slightly (by <2‰ over 30 days), yielding a value $1000\times\ln\alpha_{SO4}$ of 15.0±1.0 ‰ for the two last data points after pyrite precipitation. Only three isotope compositional data points could be obtained for S^0_{hexane} in this experiment. One data point from the first sample taken just after *T* change to 450°C (sample #4, Table 3) has an anomalously light isotope signature relative to sulfide ($1000\times\ln\alpha_{S^0}$ = -11.6 ‰). Such a low value is unlikely to be an analytical artifact, since it is in good agreement with that calculated using sulfur mass and isotope balance on sulfate and sulfide (Fig. 5a, Appendix A5). The two other S^0 isotope data points, obtained in samples #8 and #9 taken respectively 2 and 5 days after the HCl injection at 450°C (stage m32/3), show $1000\times\ln\alpha_{S^0}$ values tending to zero. The isotope composition of the precipitated pyrite in this experiment is similar to that of the aqueous sulfide fraction within 0.4 ‰ of $\delta^{34}S$ (Table 4).

Sulfur isotope data obtained in experiment m33 (Table 3, Fig. 5b,d) confirm the major isotope trends for the SO_4-H_2S pair observed in m32. The isotope composition of sulfonate (O_3-S-) and sulfane (-S) sulfur of the initial thiosulfate rapidly evolves upon heating to 300°C, with sulfate and sulfide becoming with time ^{34}S-enriched and ^{34}S-depleted, respectively. The resulting $1000\times\ln\alpha_{SO4}$ value is almost constant over the run duration, yielding a steady state value of 20.1±1.5 ‰ (Fig. 5d).

In all performed experiments, the values of $\Delta^{33}S$ for all species vary between -0.02 ‰ and +0.08 ‰, and do not show any systematic trends (Fig. 6, 7, A4.2). The values of $\Delta^{36}S$ vary between -1‰ and +1‰ without displaying any systematic trends amongst sulfide, sulfate and S^0, and overlapping with those of the initial thiosulfate. The scatter is mostly due to analytical issues because the analysis of $\delta^{36}S$ would commonly be affected by a small contribution of fluorocarbon compounds that shifts measured $\delta^{36}S$ towards more positive values (Rumble and Hoering, 1994). Nevertheless, these relatively small variations imply that there is no significant sulfur mass independent fractionation on both ^{33}S and ^{36}S; however, they do provide additional insight into both equilibrium and kinetic processes affecting mass-dependent fractionation among the sulfur species as will be discussed in section 4.2.4.

4. DISCUSSION

4.1. Solubility and chemical speciation of sulfur

Sulfur solubility and species concentrations measured in this study can be compared with equilibrium thermodynamic calculations. In all experiments, four major types of S chemical forms predicted by the available thermodynamics (Table A2.1) are aqueous sulfate (SO_4^{2-}, HSO_4^-, KSO_4^-, and $KHSO_4^0$), sulfide (H_2S, HS^-, and KHS^0), radical ions ($S_3^{\bullet-}$ at all *T*, and $S_2^{\bullet-}$ at 450°C), and pyrite (FeS_2). In addition, in m22 aqueous SO_2 and three other phases, $S_{(s,l)}$, at step m22/1, and barite ($BaSO_4$) and alunite ($KAl_3(SO_4)_2(OH)_6$) at step m22/2 after pyrite precipitation were predicted to form (Table 1). All other known solid phases are predicted to be largely undersaturated in our experiments. Other types of aqueous species, such as thiosulfate, S_8^0, and traditional polysulfide ions, represent a negligibly small amount of S_{tot} at equilibrium (<0.1%).

Comparisons between calculated and measured concentrations of sulfate, sulfide, SO_2 and S^0/ $S_3^{\bullet-}$/ $S_2^{\bullet-}$ are shown in Fig. 4; they reveal several interconnected points of discrepancy regarding the precipitation of the K_2SO_4 solid (in m32), sulfate-sulfide-pyrite equilibration, and the formation of S^0, which are discussed below.

4.1.1. K_2SO_4(s) precipitation

The precipitation of K_2SO_4(s) was inferred in run m32 (0.5 m $K_2S_2O_3$-KOH-HCl, at 300 and 450°C with in-situ changes in pH induced by HCl injection), through observation of concomitant decrease of total dissolved potassium and sulfur concentrations through time (Fig. 3c, Appendix A3). The precipitation of K_2SO_4(s) is, however, not consistent with equilibrium calculations using the thermodynamic properties of K_2SO_4(s), K^+ and sulfate aqueous species from available data sources (Table A2.1). The calculations predict K_2SO_4(s) to be undersaturated in the fluid by a factor of 10. The likely reason for this discrepancy is poor constraints on the thermodynamic parameters of the dominant KSO_4^- ion pair (Fig. 1), which are based on HKF-model extrapolations relying on limited experimental data at low temperatures. To account for K_2SO_4(s) formation, a correction to the value of the formation constant of KSO_4^- from K^+ and SO_4^{2-} at 450°C and 700 bar has been made to match the measured solubility of K_2SO_4(s) at each 450°C step of experiment m32 (log $K_{450°C,\ 700\ bar}$ = 3.4±0.5; Appendix A3). This correction does not exceed 1 log unit compared to the SUPCRT original value (log $K_{450°C,\ 700\ bar}$ = 4.4). The difference is within realistic uncertainties of HKF model predictions for such ion pairs at elevated temperatures (e.g., Pokrovski et al., 1995; Scheuermann et al., 2019). The 300°C step of this experiment does not allow direct reliable corrections for KSO_4^- formation constant, because no steady state has been attained (Fig. 3c). Therefore, we have corrected the fluid composition at the 300°C step of m32 by subtracting manually the mass-balance deduced amount of precipitated K_2SO_4, but this correction has again a minor effect (Fig. A3.2). Nevertheless, to maintain consistency, in the following discussion both 300°C and 450°C corrections were included when modeling equilibrium S speciation in experiment m32 (Fig. 4c).

4.1.2. Aqueous sulfate and sulfide and pyrite

Before the pyrite precipitation stage, a decent agreement between measured and calculated $S_{sulfide}$ values is observed for the least-concentrated experimental compositions in m29/1 (0.2 m $K_2S_2O_3$, pH ~7.3, 350°C) and m33/3 (0.2m $K_2S_2O_3$, pH ~5.3, 300°C). The other experimental compositions show systematically lower measured $S_{sulfide}$, which is due to the presence of S^0, as directly confirmed by mass balance calculations and analyses of hexane extracts (discussed in section 4.1.3 below). Another potential cause of the difference between measured and calculated $S_{sulfide}$ in the highest-temperature run (450°C, m32/2,3) might be an underestimation of the thermodynamically predicted amount of $S_2^{\bullet-}$ forming at the expense of H_2S. The measured $S_{sulfate}$ concentrations in experiments m22, m29, m33 (and m32 at 450°C, after correction for K_2SO_4(s)) agree within errors with the calculated ones, which further confirms that S^0 forms more at the expense of sulfide than sulfate. An exception to this trend is stage m32/1 at 300°C and alkaline

pH that still shows significant underestimation of measured $S_{sulfate}$, which is due to lack of equilibrium and the slowness of thiosulfate decomposition.

In the final stages of experiments m22, m29 and m32 with precipitated pyrite (and barite and alunite in m22), calculations predict almost complete scavenging of the injected Fe (and Ba) amounts by the solid phase, which is in excellent agreement with both low Fe dissolved concentrations (<0.002-0.02 m, Table 2) and the differences in $S_{sulfide}$ concentrations measured before and after the $FeCl_2$ injection. However, for all three experiments in the presence of pyrite, the measured aqueous $S_{sulfide}$ concentrations are somewhat lower than those predicted using equilibrium thermodynamics (Fig. 4a-c). The difference between measured and predicted $S_{sulfide}$ concentration values in equilibrium with pyrite (0.05-0.1 m S) suggests that pyrite, once precipitated, may not fully chemically re-equilibrate with the solution within the short time frame of these experimental stages (<10 days).

4.1.3. Molecular sulfur formation

Molecular sulfur was clearly identified in three from the four runs conducted in this study. The exception is run m29 at 350°C with the lowest S_{tot} concentration (0.4 m S), which was the simplest from the point of view of aqueous S speciation, with dominant sulfate and sulfide and negligible amounts of $S_3^{\bullet-}$ (<0.001 m S). The small imbalance between S_{tot} and [$S_{sulfide}$ + $S_{sulfate}$] in this experiment before pyrite precipitation (<0.03m S, Table 2) is comparable with the uncertainties of the species concentrations. In contrast, experiment m22, conducted at the same temperature but in a more concentrated and more acid solution, is predicted to contain at equilibrium, along with sulfate and sulfide, significant $S_3^{\bullet-}$ concentrations (0.067 m S; Table 1, Fig. 4a). The major difference between the analytical data and thermodynamic predictions for this experiment is the presence of large amounts of S^0 (~0.3 m S) as clearly apparent from mass balance between measured S_{tot} and the sum of $S_{sulfate}$ and $S_{sulfide}$ (Table 2). Such elevated S^0 concentrations are not accounted for by thermodynamics, which predicts <0.001 m of S_8^0 (aq) at equilibrium using the thermodynamic data sources from Table A2.1 (Fig. 1). The contribution from breakdown of $S_3^{\bullet-}$ to molecular sulfur on cooling during sampling can be estimated by the reaction:

$$2\ S_3^{\bullet-} + 2\ H^+ = 5\ S^0 + H_2S \qquad (9)$$

Molecular sulfur and H_2S are the most reactive S species that are known to easily form during rapid cooling of hydrothermal fluids (Giggenbach, 1997; Pokrovski and Dubessy, 2015). The formation of sulfate is kinetically too slow to occur during the sampling in our experiments (e.g., Ohmoto and Lasaga, 1982). The formation of polysulfide dianions, such as S_6^{2-} that is known to form by recombination of two $S_3^{\bullet-}$ in non-aqueous solvents (e.g., Chivers and Elder, 2013; Steudel and Chivers, 2019), is negligible at our acidic pH (Fig. 1a). Therefore reaction (9) is likely to control the $S_3^{\bullet-}$ breakdown in this experiment. Yet, the maximum produced amount of S^0 by $S_3^{\bullet-}$ breakdown in experiment m22, according to reaction (9), is 0.056 m S, which is not enough to account for the difference [S_{tot} – ($S_{sulfate}$ + $S_{sulfide}$)] in this experiment (~0.3 m S, Fig. 4a). It is thus very likely that the major part of S^0 observed in sampled fluids from this experiment has a different origin. As shown by Pokrovski and Dubessy (2015) by in-situ Raman spectroscopy on similar solutions,

another type of S^0 is present at the *T-P* conditions of this experiment and is likely represented by chain-like polymeric molecules in equilibrium with sulfate, sulfide and $S_3^{\bullet-}$ ion. Furthermore, part of S^0 found in sampled solutions in this experiment may be produced by a very fast precipitation of the native sulfur phase (S^0 liquid at >115°C and solid at lower *T*) during the sampling when the fluid is transferred from the hot reactor (350°C) to the cold sampling vial (<100°C). Indeed, thermodynamic predictions suggest that, if solid-solution equilibrium for sulfur is attained at 100°C during sampling, >30% of S_{tot} would precipitate as native sulfur before reaching the trapping iodine or zinc acetate solution in the vial. Even through such rapid attainment of equilibrium at low temperatures within the sampling time frame is unlikely (e.g., Ohmoto and Lasaga, 1982), this potential artifact of S precipitation could not be completely excluded, in particular in acidic systems in which sulfur solubility is lower (Fig. 1a,d), and thus may also contribute to the S^0 concentrations found in this experiment.

Further insight into the origin of molecular sulfur is gained from step m32/1 at lower *T* (300°C) and more alkaline pH (7.2). Under these conditions, sulfur solid/liquid phase precipitation during sampling on cooling is not favorable because of the greater S solubility in alkaline solutions (Fig. 1a) and much slower redox kinetics (e.g., Ohmoto and Lasaga, 1982). Thermodynamic calculations predict negligible amounts of S_8^0 (<0.001 m S) and fairly small amounts of $S_3^{\bullet-}$ (0.004 m S). These relatively small concentrations cannot account for the major fraction of S^0 observed at this stage (50% of S_{tot}, Table 2, Fig. 3c). This different type of S^0 is likely to originate from irreversible thiosulfate breakdown on heating:

$$S_2O_3^{2-} = S^0 + SO_3^{2-} \quad (10)$$

This reaction is the most straightforward and kinetically easiest one, since it requires only breaking the S-S bond of the thiosulfate ion with minimal electron transfer between the two S atoms. With time, both S^0 and SO_3^{2-} undergo transformation to H_2S and SO_4^{2-}, which are thermodynamically stable at these conditions:

$$4\ SO_3^{2-} + 2\ H^+ = H_2S + 3\ SO_4^{2-} \quad (11)$$

$$4\ S^0 + 4\ H_2O = 3\ H_2S + SO_4^{2-} + 2H^+ \quad (12)$$

This interpretation is supported by *i)* systematic positive difference between S_{red} and $S_{sulfide}$ at this stage (Table 2) pointing to the presence of an iodine-titratable S form such as SO_3^{2-}, in line with reaction (10); *ii*) decrease of the $S^0_{balance}$ concentration; and *iii*) increase of $S_{sulfate}$ and $S_{sulfide}$ with time at 300°C (Table 2, Fig. 3c) in line with reactions (11) and (12). With the *T* rise to 450°C, this type of S^0 becomes negligible, since both analyzed and mass-balance derived S^0 (0.045 m S on average, Table 2) is in excellent agreement with the amount that may be produced via collective breakdown of $S_3^{\bullet-}$ according to reaction (9) and $S_2^{\bullet-}$ according to an analogous reaction:

$$2\ S_2^{\bullet-} + 2\ H^+ = 3\ S^0 + H_2S \quad (13)$$

In contrast, in experiment m33 at lower *T* (300°C) and near-neutral pH, S^0 concentration that could be produced by $S_3^{\bullet-}$ breakdown is ~5 times lower than the concentration obtained using mass balance between measured S_{tot} and sulfate plus sulfide (0.065 vs 0.3-0.5 m S at stage m33/1). This imbalance indicates the presence of far more significant amounts of S^0, confirmed by direct analyses of hexane extracts (Table 2; Fig. 4d). This additionally formed S^0 observed in the sampled fluids may potentially be due to precipitation

of liquid/solid S^0 on cooling via partial recombination of sulfate and sulfide via the reversal of reaction (12), and/or via the breakdown of the polysulfide dianions (S_n^{2-}):

$$S_n^{2-} + 2H^+ = (n\text{-}1)\ S^0_{s,l} + H_2S \quad (14)$$

Indeed, S_n^{2-} ions, being negligible at our experimental temperatures of ≥ 300°C (<0.001m S), are predicted to form in increasing amounts upon equilibrium cooling for this experimental composition (up to 0.1m S at <100°C, Fig. 1d). It is impossible, however, to evaluate the exact extent of both reactions (12) and (14), which are unlikely to attain equilibrium during the fast sampling and cooling of the fluid. Subsequent dilution with water yielded a significant decrease in both S^0_{hexane} and $S^0_{balance}$ concentrations, but they are still systematically higher than the S^0 concentrations that may be produced on cooling from thermodynamically predicted $S_3^{\bullet-}$ amounts (reaction 9). The second dilution with water further decreased the observed S^0 concentrations that became with time almost identical to those predicted from $S_3^{\bullet-}$ at the end of the last stage of this experiment (~0.01 m S, Table 1).

In summary, molecular sulfur found in our experiments is only significant at rather high S_{tot} concentrations (>0.4-0.5 m) and moderate temperatures (<350°C). It may stem from multiple contributions, as summarized in Fig. 9: *i)* equilibrium chain-like S^0 forming at elevated temperatures as found by in-situ Raman spectroscopy; *ii)* S^0 formed by the fast breakdown of $S_3^{\bullet-}$ (and $S_2^{\bullet-}$) during cooling (reactions 9 and 13); *iii)* liquid or solid $S^0_{s/l}$ directly precipitated during fluid extraction from the reactor before reaching the sample vial, probably by reverse of reaction (12) and/or by reaction (14); and *iv)* S^0 as an intermediate forming at the initial stages of the thiosulfate breakdown (reaction 10). In contrast, at lower S_{tot} concentrations (<0.4 m) and/or higher temperatures (450°C), the $S_3^{\bullet-}$ (and potentially $S_2^{\bullet-}$) is the major source of the measured S^0 in our quenched samples (reactions 9 and 13). These different types of S^0 may be expected to have distinct isotope signatures, which may allow their better identification, as discussed below.

4.2. Sulfur isotope fractionation and comparison with literature data

The experimental and modelled data on S speciation in our experiments allow the interpretation of S isotope fractionation between the major aqueous and solid species, and the evaluation of the effect of the radical ions and S^0 on this fractionation.

4.2.1. Sulfate and sulfide

In all experiments, sulfate is systematically enriched in ^{34}S compared to the coexisting sulfide, in agreement with general concepts of isotope fractionation that more oxidized S atoms such as in SO_4^{2-} having stronger chemical bonds are enriched in the heavier isotope compared to more reduced and more weekly bonded S atoms such as H_2S (e.g., Urey, 1947). Isotope fractionation between sulfate and sulfide, $1000\times\ln\alpha_{SO_4} = \delta^{34}S_{sulfate} - \delta^{34}S_{sulfide}$, is 20.3±1.5 ‰ (m33, 300°C), between 14 and 21‰ (m22 and m29, 350°C), and 15.1±0.2‰ (m32/2-4, 450°C). These values are in agreement with literature data at equilibrium

from both theory and experiment (Ohmoto and Rye, 1979; Ohmoto and Lasaga, 1982; Ono et al., 2007; Otake et al., 2008; Syverson et al., 2015; Eldridge et al., 2016; references therein), which are in the range 20-24 (300°C), 17-20 (350°C), and 13-16 ‰ (450°C). In contrast, at 300°C and alkaline conditions (m32/1, pH=6.9) after 13 days of reaction, the value of $1000\times\ln\alpha_{SO_4}$ is only ~12 ‰, which is much smaller than its equilibrium counterpart of 20-24 ‰. Whereas the $\delta^{34}S_{sulfide}$ (ZnS) value becomes constant after 3 days of reaction, the corresponding $\delta^{34}S_{sulfate}$ ($BaSO_4$) value continues to steadily increase over the duration of this step (Table 3), causing $1000\times\ln\alpha_{SO_4}$ values to increase (Fig. 5a,c). A similar trend is observed at the same T (m33) but more acidic pH (5.3), with a faster reach of a steady state (Fig. 5b,d). The increasing $\delta^{34}S_{sulfate}$ values through time while $\delta^{34}S_{sulfide}$ remained constant imply another S isotope reservoir in this system that is being depleted in ^{34}S. Such a reservoir is consistent with the detection of significant amounts of S^0. The kinetic isotope patterns observed here are in agreement with the generally slow rates of isotopic equilibration of sulfate (Ohmoto and Lasaga, 1982; references therein), and attest for much higher chemical and isotope reactivity of H_2S and the associated reduced S species (S^0, $S_3^{\bullet-}$; Pokrovski and Dubessy, 2015). Using the rate law of Ohmoto and Lasaga (1982), the rate constant $\log_{10}k_r$ (in $hour^{-1}$) for an isotope exchange reaction between sulfide and sulfate at 300°C in these experiments was estimated to be -2.4±0.2 and -1.9±0.3 at pH 6.9 and 5.3, respectively (Fig. 5c,d and Appendix A5). The small difference in the k_r values with pH is consistent with faster kinetics of sulfate-sulfide redox exchange rates in more acidic solutions (Ohmoto and Lasaga, 1982; Kusakabe et al., 2000). Furthermore, our absolute k_r values are similar, within the uncertainties, to those predicted by Ohmoto and Lasaga (1982) based on a large set of compiled experimental data from dilute H_2S-SO_4 solutions (<0.2 m S_{tot}) at 300°C and near-neutral pH ($pH_{300°C}$ ~5 to 7) in which both S^0 and $S_3^{\bullet-}$ are negligible ($\log_{10}k_r$ ~ -3±1). Despite rather large errors associated with both measured and predicted k_r values that depend on the fluid pH, ionic strength, and the presence of alkalis, this comparison does not reveal any significant effect of S^0 and $S_3^{\bullet-}$ on the sulfate-sulfide chemical and isotope exchange rates.

4.2.2. Molecular sulfur and radical ions

This study reports the first experimental data on the S isotope composition, including both major (^{32}S and ^{34}S) and minor (^{33}S and ^{36}S) isotopes, of intermediate-valence aqueous sulfur species, radical sulfur ions and molecular sulfur of different origin in hydrothermal fluids. We will hereafter discuss the S^0 isotope data in terms of S^0-H_2S fractionation, which is expected to be much less affected by kinetic constraints than fractionations involving sulfate (e.g., Robinson et al., 1973; Kusakabe et al., 2000; Pokrovski and Dubessy, 2015).

In experiments at acidic to neutral pH (m33/2,3 at 300°C, m22/1 at 350°C, and m32/3,4 at 450°C), the measured $\delta^{34}S_{S^0}$ values are fairly close to those of sulfide (despite some data scatter caused by analytical uncertainties of the measurements of micro quantities of S^0, Table 3), yielding a mean isotope fractionation factor $1000\times\ln\alpha_{S^0}$ of 0±1 ‰ for the most robust data points. The absence of significant fractionation between S^0 and sulfide is confirmed by the few available literature data for both solid/liquid and aqueous S^0. For

example, Robinson (1973) did not observe any significant $\delta^{34}S$ changes (<0.4‰) during hydrolysis of orthorhombic sulfur (α-S_8) in water at 200-320°C, with the resulting H_2S being only slightly enriched in ^{34}S (by <2‰). Kamishny et al. (2014) investigated multiple sulfur isotope fractionations in Yellowstone hydrothermal springs (<100°C) and found that S^0 had values of $\delta^{34}S$ and $\delta^{33}S$ identical to or slightly heavier than those of H_2S (by <1‰). Rare existing theoretical studies and data compilations predict equilibrium values of $1000\times\ln\alpha_{S^0}$ close to zero at our high-temperature conditions (-0.3±0.5‰, Ohmoto and Rye, 1979; -0.7±0.1‰, Otake et al., 2008), as would be expected considering the small differences in redox state and bonding between the two compounds. Higher-order polysulfide dianions S_n^{2-} with n>4 were reported to be ^{34}S-enriched compared to HS^- in alkaline solutions at ambient *T-P* (by up to 7‰; Amrani et al., 2006). However, these anions are very minor at our conditions (Fig. 1) and the amplitude of fractionation is expected to tend closer to zero at the elevated temperatures of our experiments. More recently, the $S_3^{\bullet-}$ fractionation factor compared to H_2S ($\delta^{34}S_{S_3^{\bullet-}} - \delta^{34}S_{H_2S}$), has been reported to be about -1.0 ‰ at 450°C from quantum-chemical calculations on gas phase (Tossell, 2012). Even though associated with some simplifications, these calculations support the idea that the isotope signatures of $S_3^{\bullet-}$, S^0 and H_2S would be similar within 1 ‰ at hydrothermal conditions. Thus, molecular sulfur produced in the sampled fluids from these experiments is consistent with being derived from $S_3^{\bullet-}$ (and $S_2^{\bullet-}$ and chain-like S^0 detected by Raman spectroscopy at high *T*).

An exception to this pattern is molecular sulfur produced via slow irreversible thiosulfate breakdown in experiment m32 at 300°C and early stages at 450°C in alkaline solution. This particular type of S^0 exhibits an anomalously low fractionation factor, $1000\times\ln\alpha_{S^0}$, of -11.6 ‰ (Table 3, Fig. 5a). Despite the single S^0 isotope compositional value that could directly be measured at the early stages of this experiment, the trend of $\delta^{34}S_{S^0}$ to depletion with time shown in in Fig. 5a is confirmed by sulfur mass and isotope balance (Appendix A5). At present, we do not have a sound physical-chemical explanation of this unique isotope signature, very different from the close-to-zero S^0-H_2S isotope equilibrium fractionation value supported so far by the few available experimental and theoretical data. Thus, the anomalously light S^0 observed during thiosulfate breakdown is a new finding that may be related to previously un-recognized kinetic controls operating at far-from-equilibrium conditions and favoring enrichment of S^0 produced by irreversible reaction (10) in the lighter, i.e. generally more reactive, isotope ^{32}S. We note also that $\Delta^{33}S$ values show large variations at this step (Fig. 8a) confirming an out-of-equilibrium regime. In contrast, molecular sulfur from later stages of this experiment at more acidic pH (m32/3, samples #8 and #9, Table 3, Fig. 5a) has a $\delta^{34}S$ value identical within 1 ‰ to that of the coexisting aqueous sulfide. As it was shown above, the latter type of S^0 fraction is likely to originate from $S_3^{\bullet-}$ (and $S_2^{\bullet-}$) breakdown to S^0 and H_2S upon fluid quench according to reactions (9) and (13). Indeed, if no isotope exchange occurs during these fast reactions, the resulting measured S^0 should carry a $\delta^{34}S$ value similar to that of the radical ions.

Finally, an additional contribution to S^0 might result from direct precipitation of solid/liquid sulfur on cooling via recombination of H_2S and SO_4^{2-} according to the reverse of reaction (12) and/or via S_n^{2-}

breakdown via reaction (14), both leading to formation of $S^0_{s,l}$. This was likely the case for the early stage of experiment m33 before dilution with water (m33/1, samples #2 and #3, Tables 2 and 3, Fig. 5d). The two measured $1000\times\ln\alpha_{S^0}$ values are ~2.7 ‰, which may suggest a contribution from the isotopically heavier sulfate to the S^0 formation in this run. Indeed, combining an average value for $\delta^{34}S_{H_2S}$ and $\delta^{34}S_{SO_4}$ of -7 and +15 ‰, respectively, for these samples with the stoichiometry of reaction (12), and assuming that no isotope exchange has time to occur during quenching, yields $1000\times\ln\alpha_{S^0} = +2$ ‰, in fair agreement with the measured values (Fig. 5d). Similarly, polysulfide ions that were shown to be ^{34}S enriched compared to H_2S and S^0 at ambient conditions (by ~3 ‰, Amrani and Aizenshtat, 2004; Amrani et al., 2006) may partly be responsible for the slightly heavier S^0 isotope signatures, but their exact contribution is impossible to quantify because the extent of reaction (14) during the fast fluid sampling is not known. With further dilution by water in this experiment, the degree of supersaturation with respect to $S^0_{(s,l)}$ in the sampled fluid is significantly reduced, making both reactions (12) and (14) less favorable. Consequently, the measured $1000\times\ln\alpha_{S^0}$ values (for most robust analytical data points) tend to zero at these steps (m33/2,3), since this type of S_0 is mostly produced by decomposition of $S_3^{\bullet-}$ on cooling, similar to experiment m32 at 450°C discussed above. A schematic summary of S^0 isotope signatures resulting from different formation pathways is shown in Fig. 9. Thus, the isotope signature of S^0 formed in a cooling hydrothermal fluid may directly reflect sulfur chemical speciation at high *T-P* and the dynamics of speciation changes upon fluid evolution.

4.2.3. Pyrite

Sulfur isotope systematics of the precipitated pyrite exhibits a significant variability among the experiments, which may reflect the differences in aqueous S speciation, fluid acidity, temperature and duration. All these factors potentially affect both equilibrium and kinetic fractionation and pathways of FeS_2 precipitation, even though the interpretation is complicated by the impossibility to sample precipitated pyrite for simultaneous measurement of both aqueous sulfur and pyrite isotope values. Other issues add to this complexity such as *i)* relatively short durations of the post-precipitation stage (6-14 days), *ii)* paucity of isotope data for early experiments (m29), and *iii)* variations of $\delta^{34}S_{sulfide}$ in the course of the runs likely due to analytical issues. In the light of these limitations, we have chosen to use the average value of the $\delta^{34}S_{sulfide}$ data points analyzed in sampled fluids before and after pyrite precipitation (where available) in the discussion of the pyrite-aqueous sulfide fractionation factors in each experiment, as summarized in Table 4.

The average values of the pyrite-sulfide fractionation factor $1000\times\ln\alpha_{Py}$ found in the two 350°C experiments, range from -0.5±1.3 ‰ (m22, pH change upon pyrite precipitation from 4.5 to 3.7) to 1.5±0.9 ‰ (m29, pH change upon pyrite precipitation from 7.3 to 5.3), whereas in the 450°C experiment (m32, pH change from 6.8 to 5.9) it is close to zero, 0.3±0.7 ‰ (Table 4). Equilibrium $1000\times\ln\alpha_{Py}$ values reported in the literature on the basis of theoretical estimations within the range 350-450°C (Ohmoto and Rye, 1979; Otake et al., 2008; Blanchard et al., 2009; Eldridge et al., 2016) are in the range 0.5-1.0 ‰ for the Py-H_2S pair and 2.4-3.3 ‰ for the pyrite-HS^- pair, with aqueous H_2S being slightly enriched in ^{34}S compared to HS^-,

as also confirmed by recent direct experiments at ambient temperatures (Sim et al., 2019). Thus, our measured $1000\times\ln\alpha_{Py}$ value of 1.5 ‰ from the higher-pH experiment at 350°C (m29) with comparable fractions of H_2S and HS^- in the fluid before pyrite precipitation, is in reasonable agreement with those predictions. In contrast, for a more acidic (i.e. H_2S-dominated) and S^0 and $S_3^{\bullet-}$-richer experiment at the same temperature (m22), the mean $1000\times\ln\alpha_{Py}$ value of -0.5 ‰ is by ~2 ‰ lower than the theoretical estimations above for the pyrite-H_2S pair. However, these differences should be interpreted with caution because of the large uncertainty caused by variations of the $\delta^{34}S_{sulfide}$ values in the fluid before and after pyrite precipitation (Tables 3 and 4). For the 450°C experiment (m32) at near-neutral pH, our $1000\times\ln\alpha_{Py}$ value of 0.3 ‰ is identical within analytical errors to the theoretical predictions (0.5±0.5 ‰).

The $1000\times\ln\alpha_{Py}$ values of -0.5 to 0.3 ‰ for the H_2S-dominated runs (m22, m32) are only ~1 ‰ higher on average than those reported by Syverson et al. (2015) from long-duration (>100 days) fluid-pyrite exchange experiments in more dilute and more acidic (pH<2) H_2S-HSO_4^- solutions, in which both S^0 and $S_3^{\bullet-}$ are negligible. Their experimental approach used 3-isotope systematics, convincingly demonstrating attainment of isotope equilibrium between pyrite and H_2S, with $1000\times\ln\alpha_{Py}$ of -1.9±0.8 ‰ at 350°C and -1.0±0.5 ‰ at 450°C (the latter value is estimated in this study by extrapolation assuming a *T*-dependence for $1000\times\ln\alpha_{Py}$ as in Ohmoto and Rye, 1979). The 1 ‰ difference between our and Syverson et al.'s (2015) experimental values may be due to multiple factors, such as *i)* lack of pyrite-fluid isotope equilibrium in our short-duration experiments, and *ii)* different reaction pathways of pyrite formation caused by differences in S aqueous speciation and fluid pH (this study and Ohmoto and Lasaga, 1982), or degree of solution oversaturation with respect to pyrite that may lead to different crystal morphology (e.g., Murowchick and Barnes, 1986, 1987) and, potentially, S isotope fractionation during crystal growth of different crystallographic faces. All these factors may potentially cause variations of isotope signatures in pyrite compared to the coexisting fluid from which it forms. Unfortunately, our dataset is too meagre to draw more definitive conclusions or to attempt to discriminate amongst the different pyrite formation pathways amply debated in the literature (e.g., Schoonen and Barnes, 1991; Butler et al., 2004; Ono et al., 2007; Rouxel et al., 2008; Saunier et al., 2011).

Likewise, the existing theoretical estimates of pyrite-aqueous sulfide fractionation factors may be affected by limitations arising from the use of different approaches for calculating β-factors of aqueous species from one hand and of solid phases from the other hand (Saunier et al., 2011 and references therein). An additional limiting factor is imperfections of the theoretical models for estimating hydration energies of ions versus uncharged aqueous species (e.g., HS^- versus H_2S; Syverson et al., 2015) and, more generally, by inaccuracies in assessing thermodynamic properties of aqueous non-electrolytes, such as H_2S, in high *T*-*P* fluids (e.g., Oelkers et al., 2009; Akinfiev et al., 2015; references therein). Nevertheless, despite those experimental and theoretical limitations and the paucity of direct pyrite-fluid isotope exchange data over a wide range of temperature, acidity, and solution compositions, the main conclusion arising from this

discussion is that our results do not reveal any detectable effect of $S_3^{\bullet-}$ and S^0 on pyrite-fluid isotope exchange rates and resulting pyrite isotope signatures.

4.2.4. $\Delta^{33}S$ and $\Delta^{36}S$ systematics

The data obtained on the minor S isotopes, ^{33}S and ^{36}S, in S-rich hydrothermal fluid-pyrite systems of this study do not provide evidence for significant mass-independent fractionation. First, our $\delta^{33}S$ vs $\delta^{34}S$ data plot on a commonly reported MDF fractionation line with a slope of 0.515±0.001 (95% confidence level) for all experimental compositions and temperatures (Fig. 6a, 7a, A4.2a). Second, the majority of our $\Delta^{33}S$ values plot within the area outlining potential variations of the λ33 value (Fig. 6b, 7b, A4.2b) predicted among different sulfur aqueous species at equilibrium using Density Functional Theory (DFT) calculations ($0.505<\lambda33<0.517$, Otake et al., 2008; Eldridge et al., 2016) and those recorded in biological and inorganic reactions among traditional S species both in nature and experiments ($0.508<\lambda33<0.519$; LaFlamme et al., 2018a and references therein). Similarly, the most reliable $\Delta^{36}S$ values plot within the area of the theoretical λ36 slopes for MDF fractionation among S aqueous species (Fig. 6c, 7c, A4.2c; $1.88<\lambda33<1.96$; Otake et al., 2008; Eldridge et al., 2016). Third, our $\Delta^{36}S$-$\Delta^{33}S$ data do not plot on the MIF Archean array (Fig. 6d, 7d and A4.2d).

Thus, within the experimental uncertainties, our data on ^{33}S and ^{36}S may be treated in terms of MDF, and therefore may provide additional constraints on both kinetics and equilibrium of sulfur isotope exchange reactions. We followed the approach based on the assumption that the difference of $\Delta^{33}S$ and $\Delta^{36}S$ values between the different S species, being initially at disequilibrium, should tend to close-to-zero values when approaching equilibrium (Ono et al., 2007; Syverson et al., 2015; Dauphas and Schauble, 2016), provided there is no additional MIF contributions. Indeed, the most recent theoretical work of Eldridge et al. (2016) predicts equilibrium $\Delta^{33}S$ <0.01 ‰ for the SO_4^{2-}-HS^- pair at 300°C and even smaller values (<0.001 ‰) for other ionic S species. Our analysis here is limited by consideration of sulfate and sulfide, since no such theoretical predictions exists for S^0, radical ions or pyrite.

Figure 8 shows the difference in $\Delta^{33}S$ and $\Delta^{36}S$ values between aqueous sulfate and sulfide (defined hereafter as $\Delta^{33}S_{sulfate\text{-}sulfide}$ and $\Delta^{36}S_{sulfate\text{-}sulfide}$) as a function of time in each stage of experiments m32 and m33. It can be seen that at 300°C during the initial thiosulfate breakdown (m32), the $\Delta^{33}S_{sulfate\text{-}sulfide}$ and $\Delta^{36}S_{sulfate\text{-}sulfide}$ values increase with time, consistent with the absence of equilibrium at this first stage as shown by the temporal changes of both S chemical speciation and $1000\times\ln\alpha_{SO4}$ values (Fig. 5). The temperature rise to 450°C (m32) results in a decrease of $\Delta^{33}S_{sulfate\text{-}sulfide}$ and $\Delta^{36}S_{sulfate\text{-}sulfide}$ values, most of which being between 0.00 and 0.02 ‰ (Fig. 8a,b). Even though our first data are not precise enough to fully support those calculated by Eldridge et al. (2016), our trend is in line with the tendency for isotope equilibration at higher *T* shown by the $1000\times\ln\alpha_{SO4}$ evolution during the following stages (Fig. 5). Thus, our $\Delta^{33}S$ data provide additional support for the attainment of sulfate-sulfide (-pyrite) equilibrium in this experiment as independently inferred from the $\delta^{34}S$ data (Fig. 5a, A4.2). The values of $\Delta^{36}S_{sulfate\text{-}sulfide}$, which have been

obtained for the first time on such S-bearing hydrothermal systems, also indicate a tendency of approaching zero with time in the 450°C stages of experiment m32, in spite of the intrinsically large uncertainties (Fig. 8b).

Values of $\Delta^{33}S$ in the experiment at 300°C at near-neutral pH (m33) show roughly similar amplitude and pattern as in run m32, by tending towards zero during breakdown of the initial thiosulfate within the first 2 weeks (Fig. 8c). Injection of water results in a 'perturbation' of $\Delta^{33}S$ values, likely caused by partial decomposition of $S_3^{\bullet-}$ and S^0 upon dilution. Values of $\Delta^{36}S$ in this experiment are more scattered, but yet indicate a similar pattern upon water injection. Thus, our study confirms previous experimental and natural findings (e.g., Ono et al., 2007; Syverson et al., 2015; McDermott et al., 2015) that $\Delta^{33}S$ and, potentially, $\Delta^{36}S$ systematics may reflect the dynamics of sulfur species transformation and exchange in hydrothermal fluids.

5. GEOCHEMICAL SIGNIFICANCE AND PERSPECTIVES

5.1. Implications for tracing hydrothermal processes

The present study is the first experimental investigation of the effect of intermediate-valence polymeric sulfur species on S isotope fractionation involving the four stable S isotopes at conditions typical of hydrothermal S-bearing fluid circulation and metal ore formation in the shallow crust (<2-3 km) leading to various types of deposits. Our findings have several implications for using S isotopes as tracers of hydrothermal processes in the Earth's crust.

First, our data on S-rich fluids in the system pyrite-sulfide-sulfate quantitatively confirm the mass-dependent equilibrium fractionation amplitudes and kinetic patterns among these major sulfur chemical forms, previously established on the basis of extensive experimental and natural data obtained from more dilute S-poor fluids in which these polymeric sulfur species are negligible. Thus, with the available dataset, our results do not support recent hypotheses that the presence of $S_3^{\bullet-}$ (and S^0) could increase the rates of thermochemical sulfate reduction (Truche et al., 2014) or control kinetic mechanisms of sulfate-sulfide exchange reactions in hydrothermal solution at acidic and neutral pH (Pokrovski and Dubessy, 2015).

Second, our study highlighted different origins of molecular sulfur in hydrothermal fluids, which may result not only from breakdown of $S_3^{\bullet-}$ (and $S_2^{\bullet-}$), but also from partial recombination of sulfate and sulfide or isotope exchange between polysulfide dianions and H_2S on cooling out of equilibrium yielding formation of liquid or solid sulfur ($S_{(s,l)}$), or by irreversible thermal decomposition of thiosulfate (S^0_{thios}). The sulfur radical ions and S^0 have isotopic signatures indistinguishable from aqueous H_2S. The $S_{(s,l)}$ phase may be slightly ^{34}S-enriched (by 2-4 ‰) compared to H_2S thereby reflecting the contribution of SO_4^{2-} or S_n^{2-} in the reaction of $S_{(s,l)}$ precipitation. In contrast, S^0_{thios} is strongly ^{34}S-depleted compared to H_2S (by as much as -12 ‰). As a result, isotope analyses of S^0 in natural hot spring discharges, which are commonly out of

892 equilibrium owing to fast temperature changes, may actually bear information about the evolution of
893 hydrothermal fluids upon their cooling and rise to the surface.

894 *Third,* our study confirms the interpretations of small $\Delta^{33}S$ and $\Delta^{36}S$ variations ($< \pm 0.1$ and $< \pm 1$ ‰,
895 respectively) in inorganic sulfur-bearing fluid - mineral (pyrite) systems as MDF in terms of reaction kinetics
896 and mixing of S reservoirs (e.g., Ono et al., 2006; Stefansson et al., 2015; Syverson et al., 2015; McDermott
897 et al., 2015; Gunnarsson-Robin et al., 2017). These variations are thus an efficient complement to the
898 traditional $\delta^{34}S$ tracer to monitor the approach to equilibrium and evolution of hydrothermal fluids and
899 mineralization in a wide range of temperatures and S concentration and chemical speciation.

900 *Finally*, our data do not reveal any systematic mass-independent fractionation (MIF) of ^{33}S in the
901 experimental S-bearing fluid-pyrite systems over a wide range of S concentrations (0.1-1 m), pH (4-8) and
902 temperatures (300-450°C), with $\Delta^{33}S$ values of any S species being 0.0±0.1 ‰. Such values fall well within
903 the traditionally accepted general MDF threshold of ±0.2 ‰ (Farquhar and Wing, 2003) and the known
904 variations of λ33 MDF slope values (e.g., Otake et al., 2008; Eldridge et al., 2016; LaFlamme et al., 2018a).
905 Thus, our results do not confirm expectations raised in a number of recent studies (e.g., Truche et al., 2014;
906 Pokrovski et Dubessy, 2015; Selvaraja et al., 2017; LaFlamme et al., 2018a,b) that $S_3^{\bullet-}$, being a radical, might
907 generate a significant mass-independent fractionation, in addition to the widely recognized processes of SO_2
908 and other gaseous S species photolysis that shall still be considered as the primary cause of sulfur MIF
909 signatures. Thus, at the current state of our knowledge, $\Delta^{33}S$ rock record continues to serve as an efficient
910 chemically conservative isotopic tracer of Archean sediment contributions as has been widely used in
911 sedimentary and ore deposit geochemistry over the last 20 years.
912

913 **5.2. Can reactions involving sulfur radical ions generate MIF in fluid-mineral systems?**

914 The data obtained in this study account neither for findings of MIF ^{33}S signatures in some post-
915 Archean magmatic-metamorphic sulfides (e.g., Farquhar et al., 2002; Bekker et al., 2009; Cabral et al., 2013;
916 Young et al., 2013; LaFlamme et al., 2018b) nor in experiments of sulfate reduction by amino-acids in
917 hydrothermal solution (Watanabe et al., 2009; Oduro et al., 2011) or liquid-phase photolysis of particular
918 organic thiol compounds (e.g., Kopf and Ono, 2012). Therefore, the question yet remains open as to whether
919 or not reactions of sulfur radical ions may generate MIF signatures in fluid-mineral systems. Several specific
920 environments in the Earth's crust may offer potential for MIF-generating reactions involving S radical
921 species. The first is TSR processes in sedimentary/metamorphic settings in which $S_3^{\bullet-}$ is expected to be
922 abundant enough above 150°C (e.g., Truche et al., 2014; Pokrovski et Dubessy, 2015; Barré et al., 2017).
923 Until now, however, no unambiguous evidence of anomalous S isotope signatures in TSR phenomena other
924 than those in the presence of amino-acids (such as glycine, Watanabe et al., 2009; Oduro et al., 2011) is
925 available so far. But experimental data at relevant *T-P* conditions are lacking in the presence of hydrocarbon
926 compounds (C_xH_y), a type of organic matter which is the most abundant in sedimentary basins. Such
927 environments may offer a large range of chemical pathways and reaction rates involving, in addition to $S_3^{\bullet-}$,

different organic S-bearing radical species (e.g., Lewan, 1998). The particularly rich chemistry of such settings enlarges the probability to find a subtle favorable interplay of kinetic factors and dynamic parameters of reactions (not too fast and not too slow; e.g., Buchachenko, 2001; 2013), and reaction mechanisms involving radical-radical pairs, molecular cages (e.g., Kopf and Ono, 2012; references therein) or specific mineral surfaces (e.g., Lasaga et al., 2008). All these factors are expected to favor magnetic isotope effects (MIE) on the nuclear-spin possessing ^{33}S. Another natural environment that might meet some of the MIE requirements is ultramarine minerals of the zeolite group that host a plethora of S species, from S^{2-} to SO_4^{2-}, including S^0 and the radical ions, stabilized in Si/Al network structure cages (e.g., Reinen and Lindner, 1999; Tauson et al., 2011), as well as $S_3^{\bullet-}$-bearing blue fluorites (Müller, 2018). Such minerals form in a wide range on hydrothermal-metamorphic conditions and may provide an efficient structural trap for S aqueous species allowing preservation of their anomalous isotope signatures. A third possible environment for MIF-generating reactions might be in magmatic-hydrothermal settings due to the presence of another radical ion, $S_2^{\bullet-}$, which forms at the expense of $S_3^{\bullet-}$ in S-rich fluids containing sulfate and sulfate at temperatures from 450°C to at least 800°C as demonstrated by in-situ Raman spectroscopy (Pokrovski and Dubessy, 2015; Colin et al., 2018, 2020; Pokrovski et al., 2019). Having a magnetic moment similarly to $S_3^{\bullet-}$, $S_2^{\bullet-}$ might potentially be capable of producing, in fluid-magma systems, MIF anomalies at least on ^{33}S, provided other factors required for MIE have been met. In addition, an improved analytical resolution on the ^{36}S non-magnetic isotope may also help discriminating the factors leading to MIF. For example, the $\Delta^{33}S/\Delta^{36}S$ ratio has been used to differentiate the Archean MIF array from the kinetic MDF array (e.g., Johnston, 2011; LaFlamme et al., 2018a). Verifying the hypotheses evoked above, both in nature and laboratory, would require a judicious combination of in-situ time-resolved experiments with highly sensitive analytical methods for different sulfur species and the four S isotopes in the high *T-P* fluid phase, thus posing a formidable challenge for future research in sulfur isotope geochemistry.

ACKNOWLEDGMENTS

This work was funded by the French National Research Agency (grant RadicalS - ANR-16-CE31-0017), the Institut des Sciences de l'Univers of the Centre National de la Recherche Scientifique (grants S3MIF-PNP and S3MIF2-PNP), the Institut Carnot ISIFoR (grant OrPet), and the French and Icelandic embassies (grant PHC Jules Verne TraceSulf). We thank P. Gisquet, A. Castillo, P. Besson, C. Causserand, F. Candaudap, M. Henry, T. Aigouy, L. Menjot, B.A. Killingsworth, L. Guibourdenche, P. Sans-Jofre, A. Bouyon, D. Yang, and N. Findling for their professional help with the tough hydrothermal experiments and tedious chemical and isotope analyses. We enjoyed fascinating discussions about sulfur isotopes with M. Blanchard, A. Borisova, A. Buchachenko, M. Fiorentini, F. Poitrasson, J. Schott, A. Stefânsson, and L. Truche. Constructive comments of Associate Editor S. Ono, reviewers D. Syverson, H. Ohmoto, C. LaFlamme and two anonymous referees greatly improved this article.

REFERENCES

Akinfiev N.N. and Diamond L.W. (2003) Thermodynamic description of aqueous nonelectrolytes over a wide range of state parameters. *Geochim. Cosmochim. Acta* 67, 613-627.

Akinfiev N.N., Plyasunov A.V. and Pokrovski G.S. (2015) An equation of state for predicting the thermodynamic properties and vapour-liquid partitioning of aqueous $Ge(OH)_4$ in a wide range of water densities. *Fluid Phase Equil.* **392**, 74-83.

Amrani A. and Aizenshtat Z. (2004) Mechanisms of sulfur introduction chemically controlled: $\delta^{34}S$ imprint. *Org. Geochem.* **35**, 1319-1336.

Amrani A., Kamyshny Jr. A., Lev. O., Aizenshtat Z. (2006) Sulfur stable isotope distribution of polysulfide anions in an $(NH_4)_2S_n$ aqueous solution. *Inorg. Chem*. **45**, 1427-1429.

Babikov D., Kendrick B.K., Walker R.B., Schinke R. and Pack R.T. (2003) Quantum origin of an anomalous isotope effect in ozone formation. *Chem. Phys. Lett.* **372**, 686-691.

Balan E., Cartigny P., Blanchard M., Cabaret D., Lazzeri M. and Mauri F. (2009) Theoretical investigation of the anomalous equilibrium fractionation of multiple sulfur isotopes during adsorption. *Earth Planet. Sci. Lett.* **284**, 88-93.

Barré G., Truche L., Bazarkina E.F., Michels R. and Dubessy J. (2017) First evidence of the trisulfur radical ion S_3^- and other sulfur polymers in natural fluid inclusions. *Chem. Geol.* **462**, 1-14.

Bekker A., Holland H.D., Wang P.-L., Rumble III D., Stein H.J., Hannah J.L., Coedzee L.L. and Beukes N.J. (2004) Dating the rise of atmospheric oxygen. *Nature* **427**, 117-120.

Bekker A., Barley M.E., Fiorentini M.L., Rouxel O.J., Rumble D. and Beresford S.W. (2009) Atmospheric sulfur in Archean komatiite-hosted nickel deposits. *Science* **326**, 1086-1089.

Blanchard M., Poitrasson F., Meheut M., Lazzeri M., Mauri F. and Balan E. (2009) Iron isotope fractionation between pyrite (FeS_2), hematite (Fe_2O_3) and siderite ($FeCO_3$): A first-principles density functional theory study. *Geochim. Cosmochim. Acta* **73**, 6565-6578.

Buchachenko A.L. (2001) Magnetic isotope effect: nuclear spin control of chemical reactions. *J. Phys. Chem.* **A 105**, 9995-10011.

Buchachenko A.L. (2001) Mass-independent isotope effects. *J. Phys. Chem.* **B 117**, 2231-2238.

Butler I.B., Böttcher M.E., Rickard D. and Oldroyd A. (2004) Sulfur isotope partitioning during experimental formation of pyrite via polysulfide and hydrogen sulfide pathways: implications for the interpretation of sedimentary and hydrothermal pyrite isotope records. *Earth. Planet. Sci. Lett*. **228**, 495-509.

Cabral R.A., Jackson M.G., Rose-Koga E.F., Koga K.T., Whitehouse M.J., Antonelli M.A., Farquhar J., Day J.M.D. and Hauri E.H. (2013) Anomalous sulphur isotopes in plume lavas reveal deep mantle storage of Archaean crust. *Nature* **496**, 490-494.

Canfield D. E., Raiswell R., Westrich J. T., Reaves C. M. and Berner R. A. (1986) The use of chromium reduction in the analysis of reduced inorganic sulfur in sediments and shales. *Chem. Geol.* **54**, 149-155.

Chakraborty S., Jackson T.L., Ahmed M. and Mark H. Thiemens M.H. (2013) Sulfur isotopic fractionation in vacuum UV photodissociation of hydrogen sulfide and its potential relevance to meteorite analysis. *Proc. Nat. Acad. Sci*. **110**, 17650-17655.

Charlot G. (1966). *Les Méthodes de la Chimie Analytique: Analyse Quantitative Minérale*, Masson, Paris.

Chase M.W., Jr (1998) NIST-JANAF Thermochemical Tables, Fourth Edition. *J. Phys. Chem. Ref. Data, Monograph* **9**, 1-1951.

Chivers T. and Elder P.J.W. (2013) Ubiquitous trisulfur radical ion: fundamentals and applications in materials science, electrochemistry, analytical chemistry and geochemistry. *Chem. Soc. Rev.* **42**, 5996–6005.

Colin A., Pokrovski G.S., Schmidt C., Wilke M., Moyano S., Rechignat L., Bouvier P., Felix C., Hazemann J.L. and Ledé B. (2018) In situ quantification of the sulfur radical species (S_3^-, S_2^-) in aqueous fluids and silicate melts using a hydrothermal diamond anvil cell (HDAC). *J. Conf. Abstr.*, EMPG XVI, p. 55.

Colin A., Schmidt C., Pokrovski G.S., Wilke M., Borisova A.Y. and Toplis M. (2020) In-situ determination of sulfur speciation and partitioning in aqueous fluid-silicate melt systems. *Geochem. Persp. Lett.* (in press).

Dadze T.P. and Sorokin V.I. (1993) Experimental determination of the concentrations of H_2S, HSO_4^-, SO_2 aq, $H_2S_2O_3$, S^0 aq, and S total in the aqueous phase in the S-H_2O system at elevated temperatures. *Geochem. Intern.* **30**, 36-51.

Dauphas N. and Schauble E.A. (2016) Mass fractionation laws, mass-independent effects, and isotopic anomalies. *Annu. Rev. Earth Planet. Sci*. **44**, 709-783.

Delavault H., Chauvel C., Thomassot E., Devey C.W. and Dazas B. (2016) Sulfur and lead evidence of relic Archean sediments in the Pitcairn mantle plume. *Proc. Nat. Acad. Sci*. **113**, 12952-12956.

Ding T., Valkiers S., Kipphardt H., De Bièvre P., Taylor P.D.P., Gonfiantini R. and Krouse R. (2001) Calibrated sulfur isotope abundance ratios of three IAEA sulfur isotope reference materials and V-CDT with a reassessment of the atomic weight of sulfur. *Geochim. Cosmochim. Acta* **65**, 2433-2437.

Einaudi M.T., Hedenquist J.W. and Inan E.E. (2003) Sulfidation state of fluids in active and extinct hydrothermal systems: transitions from porphyry to epithermal environments (eds. S.F. Simmons and I.J. Graham). *Soc. Econ. Geol. Spec. Publ.* **10**, 285-313.

Eldridge D.L., Guo W. and Farquhar J. (2016) Theoretical estimates of equilibrium sulfur isotope effects in aqueous sulfur systems: Highlighting the role of isomers in the sulfite and sulfoxylate systems. *Geochim. Cosmochim. Acta* **195**, 171-200.

Farquhar J. and Wing B.A. (2003) Multiple sulfur isotopes and the evolution of the atmosphere. *Earth Planet. Sci. Lett.* **213**, 1-13.

Farquhar J., Bao H. and Thiemens M. (2000) Atmospheric influence of Earth's earliest sulfur cycle. *Science* **289**, 756-758.

Farquhar J., Wing B.A., McKeegan K.D., Harris J.W., Cartigny P. and Thiemens M.H. (2002) Mass-independent sulfur of inclusions in diamond and sulfur recycling on early Earth. *Science* **298**, 2369-2372.

Farquhar J., Peters M., Johnston D.T., Strauss H., Masterson A., Wiechert U. and Kaufman A.J. (2007) Isotopic evidence for Mesoarchaean anoxia and changing atmospheric sulphur chemistry. *Nature* **449**, 706-709.

Frimmel H.E. (2018) Episodic concentration of gold to ore grade through Earth's history. *Earth Sci. Rev.* **180**, 148-158.

Gao Y. and Marcus R.A. (2001) Strange and unconventional isotope effects in ozone formation. *Science* **293**, 259-263.

Geng L., Savarino J., Caillon N., Gautier E., Farquhar J., Dottin III J. W., Magalhães N., Hattori S., Ishino S., Yoshida N., Albarède F., Albalat E., Cartigny P., Ono S. and Thiemens M.H. (2019) Intercomparison measurements of two ^{33}S enriched sulfur isotope standards (2019). *J. Anal. At. Spectrom*. **34**, 1263-1271.

Giggenbach W.F. (1997) The origin and evolution of fluids in magmatic-hydrothermal systems. In: *Geochemistry of Hydrothermal Ore Deposits, 3rd edition* (ed. H. L. Barnes). John Wiley & Sons, Inc., New York, p. 737-796.

Gunnarsson-Robin J., Stefânsson A., Ono S., Torssander P. (2017) Sulfur isotopes in Icelandic thermal waters. *J. Volcan. Geotherm. Res.* **346**, 161-179.

Helgeson H.C., Kirkham D.H. and Flowers G.C. (1981) Theoretical prediction of the thermodynamic behavior of aqueous electrolytes at high pressures and temperatures: IV. Calculation of activity coefficients, osmotic coefficients and apparent molal and relative partial molal properties to 600° C and 5 kb. *Amer. J. Sci.* **281**, 1249-1516.

Hulston J.R. and Thode H.G. (1965). Variations in S^{33}, S^{34} and S^{36} contents and their relation to chemical and nuclear effects. *J. Geophys. Res*. **70**, 3475-3484.

Jacquemet N., Guillaume D., Zwick A. and Pokrovski G.S. (2014) In situ Raman spectroscopy identification of the S_3^- ion in S-rich hydrothermal fluids from synthetic fluid inclusions. *Amer. Miner.* **99**, 1109-1118.

Johnson J.W., Oelkers E.H. and Helgeson H.C. (1992) SUPCRT92: A software package for calculating the standard modal thermodynamic properties of minerals, gases, aqueous species, and reactions from 1 to 5000 bar and 0 to 1000°C. *Comput. Geosci.* **18**, 899-947.

Johnston D.T. (2011) Multiple sulfur isotopes and the evolution of Earth's surface sulfur cycle. *Earth Sci. Rev.* **106**, 161-183.

Kamyshny, A., Jr., 2008. Solubility of cyclooctasulfur in pure water and sea water at different temperatures. *Geochim. Cosmochim. Acta* **73**, 6022-6028.

Kamyshny A., Jr., Druschel G., Mansaray Z.F. and Farquhar J. (2014) Multiple sulfur isotopes fractionations associated with abiotic sulfur transformations in Yellowstone National Park geothermal springs. *Geochem. Trans.* **15**:7.

Kokh M.A., Lopez M., Gisquet P., Lanzanova A., Candaudap F., Besson P. and Pokrovski G.S. (2016) Combined effect of carbon dioxide and sulfur on vapor-liquid partitioning of metals in hydrothermal systems. *Geochim. Cosmochim. Acta* **187**, 311-333.

Kokh M.A., Akinfiev N.N., Pokrovski G.S., Salvi S. and Guillaume D. (2017) The role of carbon dioxide in the transport and fractionation of metals by geological fluids. *Geochim. Cosmochim. Acta* **197**, 433-466.

Kopf S. and Ono S. (2012) Sulfur mass-independent fractionation in liquid phase chemistry: UV photolysis of phenacylphenylsulfone as a case study. *Geochim. Cosmochim. Acta* **85**, 160-169.

Kouzmanov K. and Pokrovski G.S. (2012) Hydrothermal controls on metal distribution in Cu(-Au-Mo) porphyry systems. In: 'Geology and Genesis of Geology and Genesis of Major Copper Deposits and Districts of the World: A Tribute to Richard H. Sillitoe' (eds. J.W. Hedenquist, M. Harris, and F. Camus). *Soc. Econ. Geol. Spec. Publ.* **16**, 573-618.

Kusakabe M., Komoda Y, Takano B. and Abiko T. (2000) Sulfur isotopic effects in the disproportionation reaction of sulfur dioxide in hydrothermal fluids: implications for the $\delta^{34}S$ variations of dissolved bisulfate and elemental sulfur from active crater lakes. *J. Volcanol. Geotherm. Res*. **97**, 287-307.

Labidi J., Cartigny P., Birck J.L., Assayag N. and Bourrand J.J. (2012) Determination of multiple sulfur isotopes in glasses: A reappraisal of the MORB $\delta^{34}S$. *Chem. Geol.* **334**, 189-198.

LaFlamme C., Jamieson J.W., Fiorentini M.L., Thébaud N., Caruso S. and Selvaraja V. (2018a) Investigating sulfur pathways through the lithosphere by tracing mass independent fractionation of sulfur to the Lady Bountiful orogenic gold deposit, Yilgarn Craton. *Gondwana Res*. **58**, 27-38.

LaFlamme C., Fiorentini M., Lindsay M.D. and Bui T.H. (2018b) Atmospheric sulfur is recycled to the crystalline continental crust during supercontinent formation. *Nat. Comm.* **9**, 4380.

LaFlamme C., Sugiono D., Thebaud N., Caruso S., Fiorentini M., Selvaraja V., Jeon H., Voute F. and Martin L. (2018c) Multiple sulfur isotopes monitor fluid evolution of an Archean orogenic gold deposit. *Geochim. Cosmochim. Acta* **222**, 436-446.

Lasaga A.C., Otake T., Watanabe Y. and Ohmoto H. (2008) Anomalous fractionation of sulfur isotopes during heterogeneous reactions. *Earth Planet. Sci. Lett.* **268**, 225-238.

Laskar C., Pokrovski G.S., Kokh M.A, Hazemann J.-L., Bazarkina E.F. and Desmaele E. (2019) The impact of sulfur on the transfer of platinoïds by geological fluids. *Goldschmidt Conference 2019*, Barcelona, Spain, 1831.pdf ⟨hal-02343794⟩.

Lewan M.D. (1998) Suphur-radical control on petroleum formation rates. *Nature* **391**, 164-166.

Linke W.F. and Seidell A. (1965) *Solubilities of Inorganic and Metal-Organic Compounds: a Compilation of Solubility Data from the Periodical Literature*. 4th edition, American Chemical Society, Washington.

Masterson A.L., Farquhar J. and Wing B.A. (2011) Sulfur mass-independent fractionation patterns in the broadband UV photolysis of sulfur dioxide: Pressure and third body effects. *Earth Planet. Sci. Lett.* **306**, 253-260.

Meshoulam A., Ellis G.S., Ahmad W.S., Deev A., Sessions A.L., Tang Y., Adkins J.F., Jinzhong L., Gilhooly III W.P., Aizenshtat Z. and Amrani A. (2016) Study of thermochemical sulfate reduction mechanism using compound specific sulfur isotope analysis. *Geochim. Cosmochim. Acta* **188**, 73-92.

McDermott J.M., Ono S., Tivey M.K., Seewald J.S., Shanks III W.C., Solow A.R. (2015) Identification of sulfur sources and isotopic equilibria in submarine hot-springs using multiple sulfur isotopes. *Geochim. Cosmochim. Acta* **160**, 169-187.

Müller H. (2018) La fluorite bleuissante de Tignes, Tarentaise, Savoie. L'origine de sa coloration bleue: mise en évidence de radicaux bleus trisulfurés S_3^-. *Le Règne Minéral* **142**, 42-44 *(in French)*.

Murowchick J.B. and Barnes H.L. (1986) Marcasite precipitation from hydrothermal solutions. *Geochim. Cosmochim. Acta* **50**, 2615-2629.

Murowchick J.B. and Barnes H.L. (1987) Effects of temperature and degree of supersaturation on pyrite morphology. *Amer. Miner*. **72**, 1241-1250.

Oduro H., Harms B., Sintim H.O., Kaufman A.J., Cody G. and Farquhar J. (2011) Evidence of magnetic isotope effects during thermochemical sulfate reduction. *Proc. Nat. Acad. Sci* **108**, 17635-17638.

Oelkers E.H., Benezeth P. and Pokrovski G.S. (2009) Thermodynamic databases for water-rock interaction. In: *Thermodynamics and kinetics of water-rock interactions* (eds. E.H. Oelkers and J. Schott), Mineralogical Society of America and Geochemical Society. *Rev. Miner. Geochem.* **70**, 1-46.

Ohmoto H. and Rye R.O. (1979) Isotopes of sulfur and carbon. In *Geochemistry of Hydrothermal Ore Deposits* (H.L. Barnes ed.), Second Edition, John Wiley & Sons, 509-567.

Ohmoto H. and Lasaga A.C. (1982) Kinetics of reactions between aqueous sulfates and sulfides in hydrothermal systems. *Geochim. Cosmochim. Acta* **46**, 1727-1745.

Ohmoto H., Watanabe Y., Ikemi H., Poulson S.R. and Taylor B.E. (2007) Sulphur isotope evidence for an oxic Archaean atmosphere. *Nature* **442**, 908-911.

Ono S., Wing B., Johnston D., Farquhar J. and Rumble D. (2006) Mass-dependent fractionation of quadruple stable sulfur isotope system as a new tracer of sulfur biogeochemical cycle. *Geochim. Cosmochim. Acta* **70**, 2238-2252.

Ono S., Shanks W.S., Rouxel O.J. and Rumble D. (2007) S-33 constraints on the seawater sulfate contribution in modern seafloor hydrothermal vent sulfides. *Geochim. Cosmochim. Acta* **71**, 1170-1182.

Otake T., Lasaga C.A. and Ohmoto H. (2008) Ab initio calculations for equilibrium fractionations in multiple sulfur isotope systems. *Chem. Geol.* **249**, 357-376.

Pavlov A. and Kasting J.F. (2002) Mass-independent fractionation of sulfur isotopes in Archean sediments: strong evidence for an anoxic Archean atmosphere. *Astrobiology* **2**, 27-41.

Philippot P., van Zuilen M. and Rollion-Bard C. (2012) Variations in atmosphere sulphur chemistry on early Erath linked to volcanic activity. *Nat. Geosci.* **5**, 668-674.

Pokrovski G.S. and Dubrovinsky L.S. (2011) The S_3^- ion is stable in geological fluids at elevated temperatures and pressures. *Science* **331**, 1052-1054.

Pokrovski G.S. and Dubessy J. (2015) Stability and abundance of the trisulfur radical ion S_3^- in hydrothermal fluids. *Earth Planet Sci. Lett.* **411**, 298-309.

Pokrovski G.S., Schott J. and Sergeyev A.S. (1995) Experimental determination of the stability constants of $NaSO_4^-$ and $NaB(OH)_4^0$ in hydrothermal solutions using a new sodium selective glass electrode. Implications for boron isotopic fractionation. *Chem. Geol.* **124,** 253-265.

Pokrovski G.S., Tagirov B.R., Schott J., Hazemann J.-L. and Proux O. (2009) A new view on gold speciation in sulfur-bearing hydrothermal fluids from in situ X-ray absorption spectroscopy and quantum-chemical modeling. *Geochim. Cosmochim. Acta* **73**, 5406-5427.

Pokrovski G. S., Kokh M.A., Guillaume D., Borisova A.Y., Gisquet P., Hazemann J.-L., Lahera E., Del Net W., Proux O., Testemale D., Haigis V., Jonchière R., Seitsonen A.P., Ferlat G., Vuilleumier R., Saitta A.M., Boiron M.-C. and Dubessy J. (2015) Sulfur radical species form gold deposits on Earth. *Proc. Nat. Acad. Sci*. *USA* **112**, 13484-13489.

Pokrovski G.S., Kokh M.A., Proux O., Hazemann J.-L., Bazarkina E.F., Testemale D., Escoda C., Boiron M.-C., Blanchard M., Aigouy T., Gouy S., de Parseval P. and Thibaut M. (2019) The nature and partitioning of invisible gold in the pyrite-fluid system. *Ore Geol. Rev.* **109**, 545-563.

Reinen D. and Lindner G.-G. (1999) The nature of the chalcogen colour centres in ultramarine-type solids. *Chem. Soc. Rev*. **28**, 75-84.

Reinhardt P. and Robert F. (2013) Mass independent isotope fractionation in ozone. *Earth Planet.Sci. Lett*. **368**, 195-203.

Rielli A., Tomkins A.G., Nebel O., Brugger J., Etschmann B., Zhong R., Yaxley G.M. and Paterson D. (2017) Evidence of sub-arc mantle oxidation by sulfur and carbon. *Geochem. Persp. Lett.* **3**, 124-132.

Ripley E.M. and Li. C. (2017) A review of the application of multiple S isotopes to magmatic Ni-Cu-PGE deposits and significance of spatially variable $\Delta^{33}S$ values. *Econ. Geol.* **112**, 983-991.

Robie R.A. and Hemingway B.S. (1995) Thermodynamic properties of minerals and related substances at 298.15 K and 1 bar (10^5 Pascals) pressure and at higher temperatures. *U.S. Geol. Survey Bull.* № **2131**, 461p.

Robinson B.W. (1973) Sulphur isotope equilibrium during sulphur hydrolysis at high temperatures. *Earth Planet. Sci. Lett.* **18**, 443-450.

Rosenbauer R.J., Bischoff J.L. and Potter J.M. (1993) A flexible Au-Ir cell with quick assembly for hydrothermal experiments. *Amer. Mineral*. **78**, 1286-1289.

Rouxel O., Shanks W.C. III, Bach W. and Edwards K.J. (2008) Integrated Fe- and S-isotope study of seafloor hydrothermal vents at East Pacific Rise 9-10°N. *Chem. Geol*. **252**, 214-227.

Rumble III D. and Hoering T.C. (1994) Analysis of oxygen and sulfur isotope ratios in oxide and sulfide minerals by spot heating with a carbon dioxide laser in a fluorine atmosphere. *Acc. Chem. Res*. **27**, 237-241.

Saunier G., Pokrovski G.S. and Poitrasson F. (2011) First experimental determination of iron isotope fractionation between hematite and aqueous solution at hydrothermal conditions. *Geochim. Cosmochim. Acta* **75**, 6629-6654.

Scheuermann P. P., Tutolo B. M. and Seyfried W. E. Jr (2019). Anhydrite solubility in low-density hydrothermal fluids: Experimental measurements and thermodynamic calculations. *Chem. Geol.* **524**, 184-195.

Schoonen M.A.A. and Barnes H.L. (1991) Mechanisms of pyrite and marcasite formation from solution: III. Hydrothermal processes. *Geochim. Cosmochim. Acta* **55**, 3491-3504.

Seewald J.S. and Seyfried W.E. (1990) The effect of temperature on metal mobility in subseafloor hydrothermal systems: constraints from basalt alteration experiments. *Earth Planet. Sci. Lett*. **101**, 388-403.

Selvaraja V., Caruso S., Fiorentini M.L., LaFlamme C. K. and Bui T.H. (2017) Atmospheric sulfur in the orogenic gold deposits of the Archean Yilgarn Craton, Australia. *Geology* **45**, 691–694.

Seyfried W.E., Janecky D.R. and Berndt M.E. (1987) Rocking autoclaves for hydrothermal experiments II. The flexible reaction-cell system. In *Hydrothermal Experimental Techniques* (eds. G.C. Ulmer and H.L. Barnes). John Wiley & Sons, Inc., New York. pp. 216-239.

Shvarov Y.V. (2008) HCh: new potentialities for the thermodynamic simulation of geochemical systems offered by Windows. *Geochem. Intern.* **46**, 834-839.

Shvarov Y.V. (2015) A suite of programs, OptimA, OptimB, OptimC, and OptimS, compatible with the Unitherm database, for deriving the thermodynamic properties of aqueous species from solubility, potentiometry and spectroscopy measurements. *Applied Geochem*. **55**, 17-27.

Sim M.S., Sessions A.L., Orphan V.J. and Adkins J.F. (2019) Precise determination of equilibrium sulfur isotope effects during volatilization and deprotonation of dissolved H_2S. *Geochim. Cosmochim. Acta* **248**, 242-251.

Smit K.V., Shirey S.B., Hauri E.H. and Stern R.A. (2019) Sulfur isotopes in diamonds reveal differences in continent construction. *Science* **364**, 383-385.

Steudel R. and Chivers T. (2019) The role of polysulfide dianions and radical anions in the chemical, physical and biological sciences, including sulfur-based batteries. *Chem. Soc. Rev*. **48**, 3279-3319.

Stefànsson A., Keller N.S., Robin J.G. and Ono S. (2015) Multiple sulfur isotope systematics of Icelandic geothermal fluids and the source and reactions of sulfur in volcanic geothermal systems at divergent plate boundaries. *Geochim. Cosmochim. Acta* **165**, 307-323.

Sverjensky D. A., Harrison B. and Azzolini D. (2014) Water in the deep Earth: the dielectric constant and the solubilities of quartz and corundum to 60 kb and 1200°C. *Geochim. Cosmochim. Acta* **129**, 125-145.

Syverson D.D., Ono S., Shanks W.C. and Seyfried W.E., Jr. (2015) Multiple sulfur isotope fractionation and mass transfer processes during pyrite precipitation and recrystallization: An experimental study at 300 and 350°C. *Geochim. Cosmochim. Acta* **165**, 418-434.

Tauson V.L., Goettlicher J., Sapozhnikov A.N., Mangold S. and Lustenberg E.E. (2012) Sulphur speciation in lazurite-type minerals $(Na,Ca)_8[Al_6Si_6O_{24}](SO_4,S)_2$ and their annealing products: a comparative XPS and XAS study. *Eur. J. Miner.* **24**, 133-152.

Thode H. G., Monster J. and Dunford H. B. (1961) Sulphur isotope geochemistry. *Geochim. Cosmochim. Acta* **25**, 159-174.

Thomassot E., Cartigny P., Harris J.W., Lorand J.P., Rollion-Bard C. and Chassidon M. (2009) Metasomatic diamond growth: A multi-isotope study (^{13}C, ^{15}N, ^{33}S, ^{34}S) of sulphide inclusions and their host diamonds from Jwaneng (Botswana). *Earth Planet. Sci. Lett*. **282**, 79-90.

Tossell J.A. (2012) Calculation of the properties of the S_3^- radical ion and its complexes with Cu^+ in aqueous solution. *Geochim. Cosmochim. Acta* **95**, 79-92.

Truche L., Bazarkina E.F., Barré G., Thomassot E., Berger G., Dubessy J. and Robert P. (2014) The role of S_3^- ion in thermochemical sulfate reduction: Geological and geochemical implications. *Earth Planet. Sci. Lett.* **396**, 190-200.

Urey H. C. (1947) The thermodynamic properties of isotopic substances. *J. Chem. Soc.* (London), 562-581.

Uyama F., Chiba H., Kusakabe M. and Sakai H. (1985) Sulfur isotope exchange reactions in the aqueous system: thiosulfate-sulfide-sulfate at hydrothermal temperature. *Geochem. J.* **19**, 301-315.

Young E.D., Galy A. and Nagahara H. (2002) Kinetic and equilibrium mass-dependent isotope fractionation laws in nature and their geochemical and cosmochemical significance. *Geochim. Cosmochim. Acta* **66**, 1095-1104.

Young S.A., Loukola-Ruskeeniemi K. and Pratt L.M. (2013) Reactions of hydrothermal solutions with organic matter in Paleoproterozoic black shales at Talvivaara, Finland: Evidence from multiple sulfur isotopes. *Earth Planet. Sci. Lett.* **367**, 1-14.

Watanabe Y., Farquhar J. and Ohmoto H. (2009) Anomalous fractionations of sulfur isotopes during thermochemical sulfate reduction. *Science* **324**, 370-373.

Table 1. Summary of the experiments conducted in this study.

Run/step	Experimental system composition at each step (moles of substance/kg fluid)	$pH_{T\text{-}P}$ [a]	$pH^0_{T\text{-}P}$ [b]	*T*, °C	*P* range, bar	Duration, of step, days	Injected aqueous solution	Predicted concentration of $S_3^{\bullet-}$, mol S/kg fluid	Solid phases precipitated
m22/1	$K_2S_2O_3$(0.49), HCl(0.14), QMM [c]	4.5	5.7	350	335-370	10	-	0.067	native sulfur
m22/2	$K_2S_2O_3$(0.38), HCl(0.11), KCl(0.10), $FeCl_2$(0.18), $BaCl_2$(0.09)	3.8	5.7	350	360-380	14	KCl-$FeCl_2$-$BaCl_2$	0.0005	pyrite, barite, alunite
m29/1	$K_2S_2O_3$(0.19), KOH(0.091)	7.3	5.7	350	400-405	13	-	0.0004	-
m29/2	$K_2S_2O_3$(0.16), KOH(0.075), FeCl2(0.059)	5.3	5.7	350	380-410	6	$FeCl_2$	0.0002	pyrite
m32/1[d]	$K_2S_2O_3$(0.50), KOH(0.30)	6.9	5.5	300	430-480	13	-	0.004	-
m32/2	$K_2S_2O_3$(0.50), KOH(0.30)	7.9	6.0	450	690-725	14	-	0.007	-
m32/3	$K_2S_2O_3$(0.41), KOH(0.20), HCl (0.17)	6.8	6.0	450	705-710	8	HCl	0.037	-
m32/4	$K_2S_2O_3$(0.34), KOH(0.17), HCl (0.14), FeCl2(0.051)	5.9	6.0	450	695-720	8	$FeCl_2$	0.020	pyrite
m33/1	$K_2S_2O_3$ (0.48)	5.3	5.5	300	410-565	15	-	0.065	-
m33/2	$K_2S_2O_3$ (0.32)	5.3	5.5	300	430-550	18	H_2O	0.024	-
m33/3	$K_2S_2O_3$ (0.21)	5.3	5.5	300	380-505	8	H_2O	0.008	-

[a] Calculated pH of the fluid at each injection step at indicated *T*-*P*.
[b] Calculated pH of the neutrality point of water at indicated *T*-*P* as $a[H^+] = a[OH^-] = 0.5 \times \log_{10} K_w$, where $K_w = 1/(a_{H^+} \times a_{OH^-})$ is the water dissociation constant, and *a* is H^+ or OH^- activity.
[c] Quartz-Muscovite-Microcline mineral assemblage.
[d] The pH and $S_3^{\bullet-}$ concentration values will be slightly refined in the course of this study for experiment m32/1-4 after correction for K_2SO_4 precipitation (section 4.1.1, Fig. 4c, Appendix A3).

1234 **Table 2**. Fluid composition and sulfur speciation measured in sampled fluids from the experiments of this study.
1235

N	Duration, days	T, °C	P, bar	S_{tot}	S_{red}	$S_{sulfide}$	$S_{sulfate}$	S^0_{hexane}	$S^0_{balance}$[a]	K	Cl	Fe	K_2SO_4	Pyrite	m fluid
				mol/kg fluid									mol	mol	g
m22: $K_2S_2O_3$ (0.49 m)-HCl (0.14 m), Quartz-Muscovite-Microcline mineral assemblage															
1	1	350	370	1.01	-	0.31	0.41	-	0.29	1.00	0.13	10^{4}	-	-	150.00
2	3	350	335	1.09	-	0.31	0.43	-	0.35	1.02	0.13	$2x10^{-5}$	-	-	142.72
3	7	350	370	0.96	0.34	0.30	0.42	-	0.21	0.92	0.13	$2x10^{-5}$	-	-	136.87
4	10	350	370	0.98	0.33	0.30	0.40	-	0.26	0.97	0.13	10^{-5}	-	-	130.05
Injection of KCl-$BaCl_2$-$FeCl_2$															
5	14	350	380	0.27	0.02	<0.01	0.23	-	<0.03	0.86	0.74	0.027	-	0.028	153.19
6	17	350	370	0.28	0.02	<0.01	0.22	-	<0.04	0.88	0.74	0.023	-	0.028	144.80
7	24	350	360	0.27	0.02	<0.01	0.21	-	<0.04	0.86	0.75	0.014	-	0.028	136.83
m29: $K_2S_2O_3$ (0.19 m) - KOH (0.091 m)															
1	7	352	400	0.37	0.18	0.17	0.17	-	<0.02	0.48	0.02	$4x10^{-5}$	-	-	65.62
2	13	352	405	0.34	0.16	0.14	0.15	-	<0.03	0.48	<0.01	$5x10^{-5}$	-	-	57.57
Injection of $FeCl_2$															
3	16	352	410	0.13	<0.005	<0.01	0.14	-	<0.01	0.39	0.20	<0.002	-	0.0039	59.51
4	19	352	380	0.11	<0.005	<0.01	0.10	-	<0.01	0.39	0.19	<0.002	-	0.0039	51.73
m32: $K_2S_2O_3$ (0.50 m) - KOH (0.30 m)															
1	3	302	480	0.94	0.28	0.20	0.18	-	0.48	1.15	-	-	0.0083	-	111.23
2	8	301	430	0.89	0.31	0.20	0.17	-	0.41	1.11	-	-	0.0095	-	101.69
3	13	299	440	0.86	0.28	0.25	0.24	-	0.34	1.06	-	-	0.011	-	96.16
Temperature rise to 450°C															
4	16	451	695	0.71	0.31	0.40	0.32	0.062	<0.01	0.79	-	-	0.023	-	90.72
5	20	451	685	0.69	0.28	0.35	0.24	0.005	0.10	0.78	-	-	0.022	-	84.36
6[d]	23	453	725	0.75	0.53	-	-	-	-	0.93	-	-	0.014	-	78.02
7[d]	27	452	690	0.59	0.33	0.37	0.28	0.006	<0.01	0.60	-	-	0.026	-	75.57
Injection of HCl															
8	29	452	710	0.62	0.20	0.20	0.35	0.008	0.07	0.74	0.20	-	0.012	-	84.82
9	32	451	710	0.57	0.19	0.19	0.31	0.060	0.07	0.68	0.18	-	0.014	-	79.26
10	35	452	700	0.54	0.19	0.25	0.32	0.117	<0.01	0.61	0.22	-	0.015	-	72.16
Injection of $FeCl_2$															
11	37	452	720	0.43	0.09	0.13	0.33	0.023	<0.01	0.68	0.27	-	0.0063	0.0041	79.48
12	41	452	710	0.47	0.10	0.11	0.28	0.032	0.08	0.76	0.29	-	0.0027	0.0041	70.14
13	44	451	695	0.48	0.03	0.084	0.30	-	0.10	0.75	0.28	-	0.0028	0.0041	63.31
m33: $K_2S_2O_3$ (0.48 m)															
1	<1	300	570	0.96	0.20	0.28	0.40	0.87[b]	0.28	0.99	-	-	-	-	83.65
2	2	300	470	0.98	0.30	0.25	0.44	0.60[b]	0.24	1.02	-	-	-	-	70.28
Injection of $K_2S_2O_3$															

3	5	300	510	1.11	0.26	0.26	0.42	0.61	0.43	1.01	-	-	-	-	76.11
4	15	300	410	1.15	0.16	0.21	0.38	0.034[c]	0.56	1.07	-	-	-	-	64.99
Injection of H_2O															
5	21	300	545	0.62	0.20	0.21	0.28	0.39	0.13	0.60	-	-	-	-	84.60
6	26	300	490	0.64	0.21	0.22	0.27	0.31	0.15	0.64	-	-	-	-	77.73
7	33	300	425	0.60	0.16	0.21	0.26	0.15	0.13	0.63	-	-	-	-	69.42
Injection of H_2O															
8	35	300	505	0.42	0.15	0.14	0.19	0.14	0.08	0.44	-	-	-	-	81.00
9	37	300	440	0.42	0.12	0.16	0.19	0.013	0.07	0.43	-	-	-	-	72.71
10	41	300	380	0.38	0.13	0.14	0.22	0.005	0.02	0.39	-	-	-	-	64.87
	error	±2	±15	±10%	±10%	±20%	±15%	±50%	±30%	±5%	±10%	±10%			

"-" means not analyzed or not applicable.

S_{red} includes S species other than sulfate and molecular sulfur, which all react with iodine (sulfide, radical ions, polysulfide ions, sulfite, thiosulfate).

[a] $S^0_{balance} = S_{tot} - (S_{red} + S_{sulfate})$; if $S_{red} < S_{sulfide}$ or not available then $S_{sulfide}$ was used instead of S_{red}.

[b] Likely overestimated because of the S^0 UV signal contamination by organic impurities from the acetate decomposition.

[c] Underestimated because of insufficient time of reaction with hexane.

[d] Temperature instability due to heat regulation failure around samples #6 and #7 (see Appendix A3 for details).

1243 **Table 3.** Isotopic composition (in ‰) of sulfate (as $BaSO_4$), sulfide (as ZnS) and molecular sulfur (S^0, where available) analyzed in
1244 sampled fluids from the experiments of this study.
1245

N	Duration, days	$\delta^{34}S_{sulfide}$	$\delta^{34}S_{S^0}$	$1000\times\ln\alpha_{S^0}$	$\delta^{34}S_{sulfate}$	$1000\times\ln\alpha_{SO_4}$	$\Delta^{33}S_{sulfide}$	$\Delta^{33}S_{S^0}$	$\Delta^{33}S_{sulfate}$	$\Delta^{36}S_{sulfide}$	$\Delta^{36}S_{S^0}$	$\Delta^{36}S_{sulfate}$
m22: $K_2S_2O_3$ (0.49 m)-HCl (0.14 m), Quartz-Muscovite-Potassic feldspar mineral buffer												
1	1	-13.84	-13.87	-0.03	-	-	0.017	0.011	-	-0.51	0.16	-
2	3	-14.13	-14.15	-0.02	-	-	0.015	0.022	-	-0.39	-0.31	-
3	7	-13.86	-13.75	-0.10	-	-	0.013	0.031	-	-0.23	-0.83	-
4	10	-14.71	-14.16	0.54	-0.60[a]	14.10	0.023	0.052	0.042[a]	0.71	-0.73	-0.05[a]
Injection of KCl-$BaCl_2$-$FeCl_2$												
5	14	-12.05	-11.80	0.24	-	-	0.036	0.054	-	0.17	-0.78	-
6	17	-11.89	-13.14	-1.26	-	-	0.020	0.035	-	-0.72	-0.67	-
7	24	-12.92	-12.68	0.25	7.75	20.68	0.024	0.046	-0.024	-	0.76[e]	-
m29: $K_2S_2O_3$ (0.19 m) - KOH (0.091 m)												
1	7	-14.58	-	-	3.95	18.53	0.028	-	-	-0.72	-	-0.41
2	13	-15.01	-	-	-	-	0.034	-	-	-0.79	-	-
Injection of $FeCl_2$												
3	16	-	-	-	6.85	-	-	-	0.029	-	-	0.13
4	19	-	-	-	2.17	-	-	-	0.052	-	-	-0.58
m32: $K_2S_2O_3$ (0.50 m) - KOH (0.30 m)												
		300°C										
0	0	7.18[b]		-	-1.26[c]	N/A	0.004[b]		0.061[c]	-0.09[b]		-0.25[c]
1	3	-3.45	2.00[f]	5.45[f]	4.56	8.01	-0.001	-	0.013	-0.44	-	-0.41
2	8	-3.25	-0.50[f]	2.75[f]	8.42	11.67	0.001	-	0.051	-0.48	-	-0.40
3	13	-2.40	-4.40[f]	-2.00[f]	9.68	12.08	-0.022	-	0.069	-0.29	-	0.15
Temperature rise to 450°C												
4	16	-2.36	-13.96	-11.61	10.41	12.76	0.020	0.065	0.035	-0.44	-0.80	-0.23
5	20	-2.34	-	-	10.75	13.09	0.018	-	0.033	-0.53	-	-0.27
6	23											
7	27	-2.31	-	-	-	-	0.024	-	-	-0.46	-	-
Injection of HCl												
8	29	-2.11	-1.00	1.11	-	-	0.017	-0.016	-	-0.47	-0.02	-
9	32	-2.41	-2.40	0.01	11.30	13.71	0.013	-0.003	0.026	-0.52	-0.27	-0.19
10	35	-2.50	-		11.98	14.48	0.020	-	0.023	-0.48	-	-0.18
Injection of $FeCl_2$												
11	37	-1.26	-	-	11.24	12.50	0.011	-	0.042	-0.49	-	-0.30
12	41	-1.57	-	-	13.03	14.60	0.018	-	0.020	-0.43	-	-0.18

13	44	-1.27	-	-	13.85	15.13	0.021	-	0.022	-0.33	-	-0.16
m33: $K_2S_2O_3$ (0.48 m)												
0	0	5.37[b]	-	-	5.08[a,c]	-	0.012[b]	-	0.028[a,c]	0.45[b]	-	0.45[a,c]
1	<1	-4.93	-	-	12.93	17.86	0.004	-	0.053	0.04	-	0.11
2	2	-6.61	-3.87	2.74	11.50	18.11	0.010	0.034	0.054	0.61[d]	-0.47	-0.07
Injection of $K_2S_2O_3$												
3	5	-7.51	-4.78[e]	2.73[e]	16.61[e]	24.13[a]	0.022	0.080[e]	0.047[e]	0.28	3.51[e]	0.24[e]
4	15	-6.04	-		16.46[e]	22.50	0.025	-	0.026[e]	0.72[d]	-	5.01[e]
Injection of water												
5	21	-6.73	-7.27	-0.54	13.70	20.43	0.035	0.029	0.037	1.02[d]	-0.51	0.17
6	26	-6.32	-3.35[e]	2.97[e]	12.35	18.67	0.013	0.023[e]	0.045	-0.25	0.97[e]	0.09
7	33	-7.10	-6.59	0.51	13.41	20.51	0.031	0.004	0.050	-0.38	-0.53	0.61
Injection of water												
8	35	-7.38	-	-	11.44[e]	18.82	0.041	-	0.087[e]	-0.26	-	3.76[d,e]
9	37	-7.23	-2.41[e]	4.82[e]	14.29	21.52	0.025	0.011[e]	0.055	0.28	-0.14[e]	0.66
10	41	-8.04	-8.61	-0.57	12.37	20.40	0.024	0.010	0.027	0.13	-0.04	0.05
Error, ‰		±0.05	±0.05	±0.10	±0.05	±0.10	±0.010	±0.020	±0.02	±0.20	±0.20	±0.20

Note that two different sources of thiosulfate have been used for experiments m22 plus m29 and m32 plus m33, resulting in different $\delta^{34}S$ values relative to V-CDT.
"-"not available or analysis was judged to be unreliable.
[a] Chemical yield <10%.
[b] Ag_2S fraction of the initial $K_2S_2O_3$ corresponding to the isotope composition of the sulfane group.
[c] $BaSO_4$ fraction of the initial $K_2S_2O_3$ corresponding to the isotope composition of the sulfonate group.
[d] Error (1 SD) >0.5‰.
[e] Micro-volume measurement (<30 μg of S).
[f] Calculated values using mass and isotope balance (see Appendix A5).

Table 4. Sulfur isotope composition (in ‰) of precipitated pyrite, and pyrite-aqueous sulfide fractionation factors in the experiments of this study.

Run	*T*, °C	N_{pyrite} pts	$\delta^{34}S_{pyrite}$ [a]	$\Delta^{33}S_{pyrite}$	$\Delta^{36}S_{pyrite}$	$N_{sulfide}$ pts	$\delta^{34}S_{sulfide}$ [b]	$\Delta^{33}S_{sulfide}$	$\Delta^{36}S_{sulfide}$	$1000\times \ln\alpha_{Py}$ [c]	$\Delta^{33}S_{pyrite} - \Delta^{33}S_{sulfide}$	$\Delta^{36}S_{pyrite} - \Delta^{36}S_{sulfide}$
m22	350	2	-13.8±0.5	0.036±0.010	-0.22±0.25	6	-13.3±1.2	0.022±0.008	-0.1±0.6	-0.5±1.3	0.014±0.013	-0.13±0.60
m29	350	4	-13.3±0.5	0.046±0.007	-0.81±0.26	2	-14.8±0.8	0.031±0.004	-0.8±0.1	1.5±0.9	0.014±0.008	-0.05±0.30
m32[d]	450	1	-1.5±0.5	0.010±0.010	-0.30±0.18	6	-1.9±0.6	0.017±0.004	-0.5±0.1	0.3±0.7	-0.006±0.011	0.15±0.30

[a] $\delta^{34}S_{pyrite}$ is the average of N_{pyrite} independent IRMS measurements for the same sample (error is 1SD of the mean).
[b] $\delta^{34}S_{sulfide}$ corresponds to the $\delta^{34}S$ value of the ZnS fraction in the sampled fluid, calculated as the average of the indicated $N_{sulfide}$ number of samples taken before and after $FeCl_2$ injection for experiments m32 and m22 (3 samples before and 3 after), and before $FeCl_2$ injection for experiment m29 (2 samples).
[c] $\alpha_{Py} = \delta^{34}S_{pyrite} - \delta^{34}S_{sulfide}$.
[d] A different source of thiosulfate has been used in m32 resulting in different $\delta^{34}S$ values relative to V-CDT compared to m22 and m29.

Figure captions

Fig. 1. Sulfur species concentrations in aqueous $K_2S_2O_3$-bearing fluids representative of this study, predicted using thermodynamic modeling with available data sources (Table A2.1), at the indicated compositions as a function of pH (adjusted by adding KOH or HCl) at 300°C, 500 bar (A) and 450°C, 700 bar (B), total sulfur (S_{tot}) concentration at 300°C, 500 bar (C), and temperature at 700 bar (D). Vertical dashed lines in (A) and (B) indicate the pH of the neutrality point of water at the given *T* and *P*; vertical dotted lines show approximate compositions of our experiments (see Table 1 and Fig. 4 for calculations at specific compositions of each experimental step; note that experiments m22 and m29 carried out at 350°C are indicated in (A) for the sake of completeness). The oxygen fugacity is indicated relative to the hematite-magnetite buffer (HM, in log units).

Fig. 2. Sequence of the experimental procedures of this study using the flexible-cell hydrothermal reactor.

Fig. 3. Evolution of sulfur speciation in the fluid with time in experiments performed in this study (m22, m29, m32, and m33). S_{total}, $S_{sulfide}$, $S_{sulfate}$ and S^0_{hexane} denote analyzed concentrations whereas $S^0_{balance}$ is the difference in S concentration between measured S_{tot} and (S_{red} + $S_{sulfate}$). Dashed vertical lines show the time of in-situ injection into the reactor of the indicated aqueous solutions (see Table 1 and 2 for the exact fluid compositions).

Fig. 4. Comparisons between experimentally measured aqueous sulfate and sulfide concentrations and the corresponding thermodynamically predicted values, and between mass-balance derived molecular sulfur ($S^0_{balance}$) and thermodynamically predicted $S_3^{\bullet-}$ (plus $S_2^{\bullet-}$ at 450°C), at each sampling point of the four conducted experiments. Calculations for m32 (C) take into account corrections for K_2SO_4 precipitation and stability constant of KSO_4^- (see Appendix A3).

Fig. 5. Values of $\delta^{34}S$ (‰) of the indicated aqueous S species and pyrite and the corresponding isotope fractionation factor (α, relative to sulfide) of sulfate, S^0 and pyrite as a function of time in experiment m32 (A and C) and m33 (B and D). The dotted curve and 4 cross symbols in (A) show the evolution of S^0 isotope composition calculated using sulfur mass and isotope balance (see Appendix A5). The dotted curves (±1 SD) in (C and D) show a fit of experimental points at 300°C using the rate law from Ohmoto and Lasaga (1982): $2.303\times\log_{10}((\alpha_e-\alpha)/(\alpha_e-\alpha_0)) = -k_r\times t\times([\Sigma SO_4^{2-}]+[\Sigma S^{2-}])$, where *t* is the reaction time (in days); α_0, α and α_e are the fractionation factors of sulfate, respectively, at t=0 (initial condition), during the course of reaction, and at equilibrium; and $[\Sigma SO_4^{2-}]+[\Sigma S^{2-}]$ is the sum of concentrations of sulfate and sulfide species. The equilibrium fractionation factor ($1000\times\ln\alpha_e$ = 20.2 ‰) was taken from Ohmoto and Lasaga (1982). The fractionation factors $1000\times\ln\alpha_0$ at t=0 for m32 and m33 are 6.0±1.0 and 17.5±1.0 ‰, respectively, as estimated from time-series fractionation data points regressed to zero. Fitting the 3 data points (m32) and 9 data points (m33, by excluding a single outlier from this trend, $1000\times\ln\alpha_{SO_4}$ ~24 ‰, sample #3, which might be due to analytical issues related to a low SF_6 fluorination yield) at 300°C for α yields a $\log_{10}k_r$ value (in $hour^{-1}$) of -2.4±0.2 (pH 6.9, m32) and -1.9±0.3 (pH 5.3, m33), respectively.

Fig. 6. Isotope composition of the indicated sulfur species in samples from experiment m32 ($K_2S_2O_3$-KOH-HCl; 300 and 450°C). Uncertainties of the coefficients of the linear regression equation in (A) are given for 95% confidence level (2 SD). The lower and upper limits of the reported λ33 (from 0.505 to 0.519) and λ36 (from 1.88 to 1.96) MDF slopes that encompass both equilibrium ab-initio calculated (Otake et al., 2008, for λ33 and λ36) and experimental and natural equilibrium and kinetic (LaFlamme et al., 2018a; references therein, for λ33) variations are shown in (B) and (C) by the blue area within which most of datapoints fall (except only few outliers for sulfate and sulfonate S that are very likely to be related to analytical difficulties of $BaSO_4$ conversion). The MDF $\Delta^{36}S$ vs $\Delta^{33}S$ array (*MDF-S*, slope of -9 to -7) and the Archean MIF array (*MIF-S*, slope of -2 to -1) according to Johnston (2011) are shown in (D).

Fig. 7. Sulfur isotope compositions of the indicated species in samples from experiment m33 ($K_2S_2O_3$; 300°C). See Fig. 6 caption for details about the plots.

Fig. 8. The difference of $\Delta^{33}S$ and $\Delta^{36}S$ values for the sulfate-sulfide pair as a function of time in experiments m32 and m33. Gray symbols at time 0 indicate the difference values for the sulfonate-sulfane pair in the initial thiosulfate.

Fig. 9. Schematic summary of the formation mechanisms of molecular sulfur in hydrothermal fluids and associated sulfur isotope fractionation between the resulting S^0 and aqueous sulfide ($1000\times\ln\alpha_{S^0} \approx \delta^{34}S_{S^0} - \delta^{34}S_{sulfide}$) identified in this study. Blue and red arrows indicate, respectively, fluid cooling and heating.

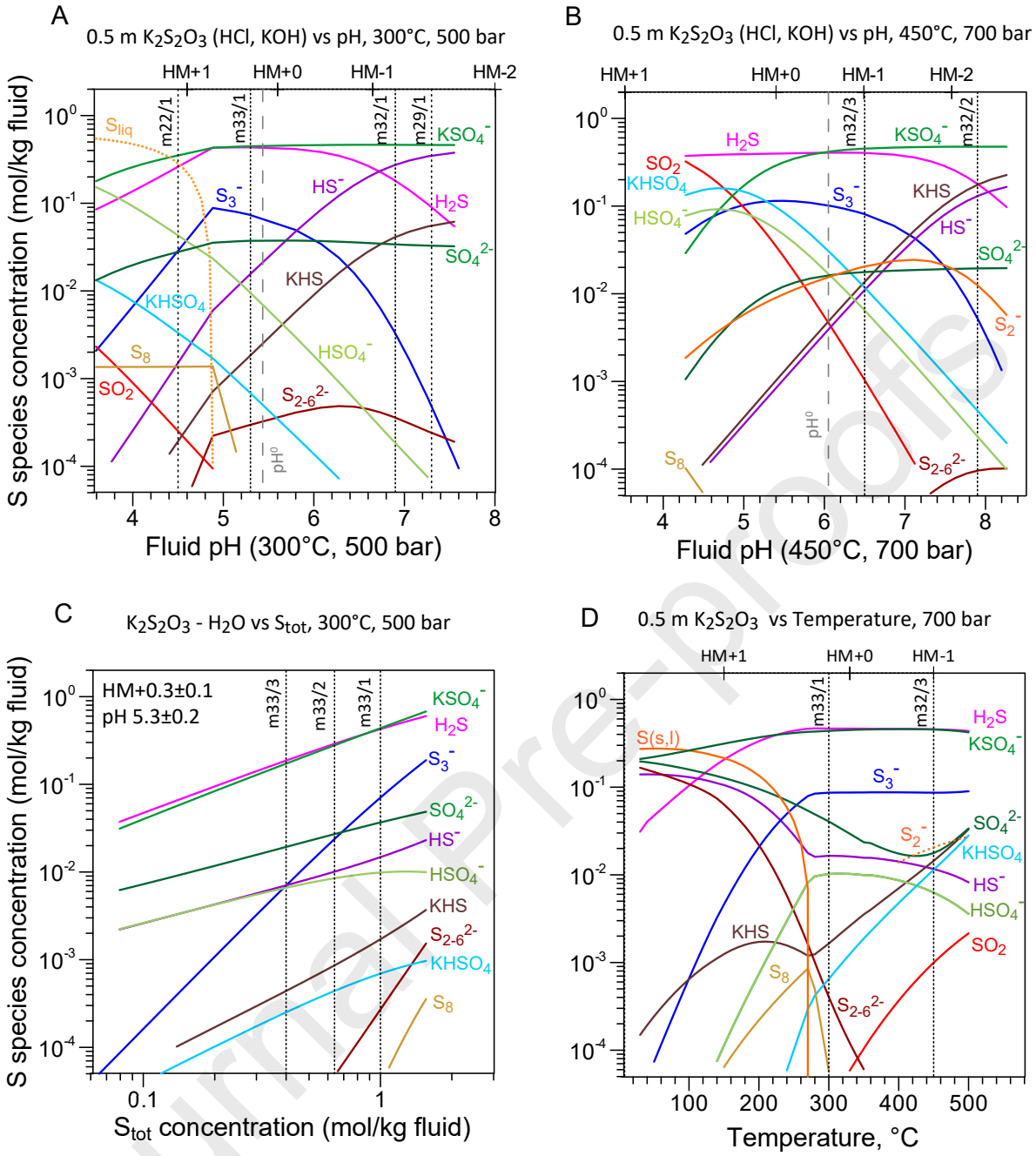

Fig. 1

1334

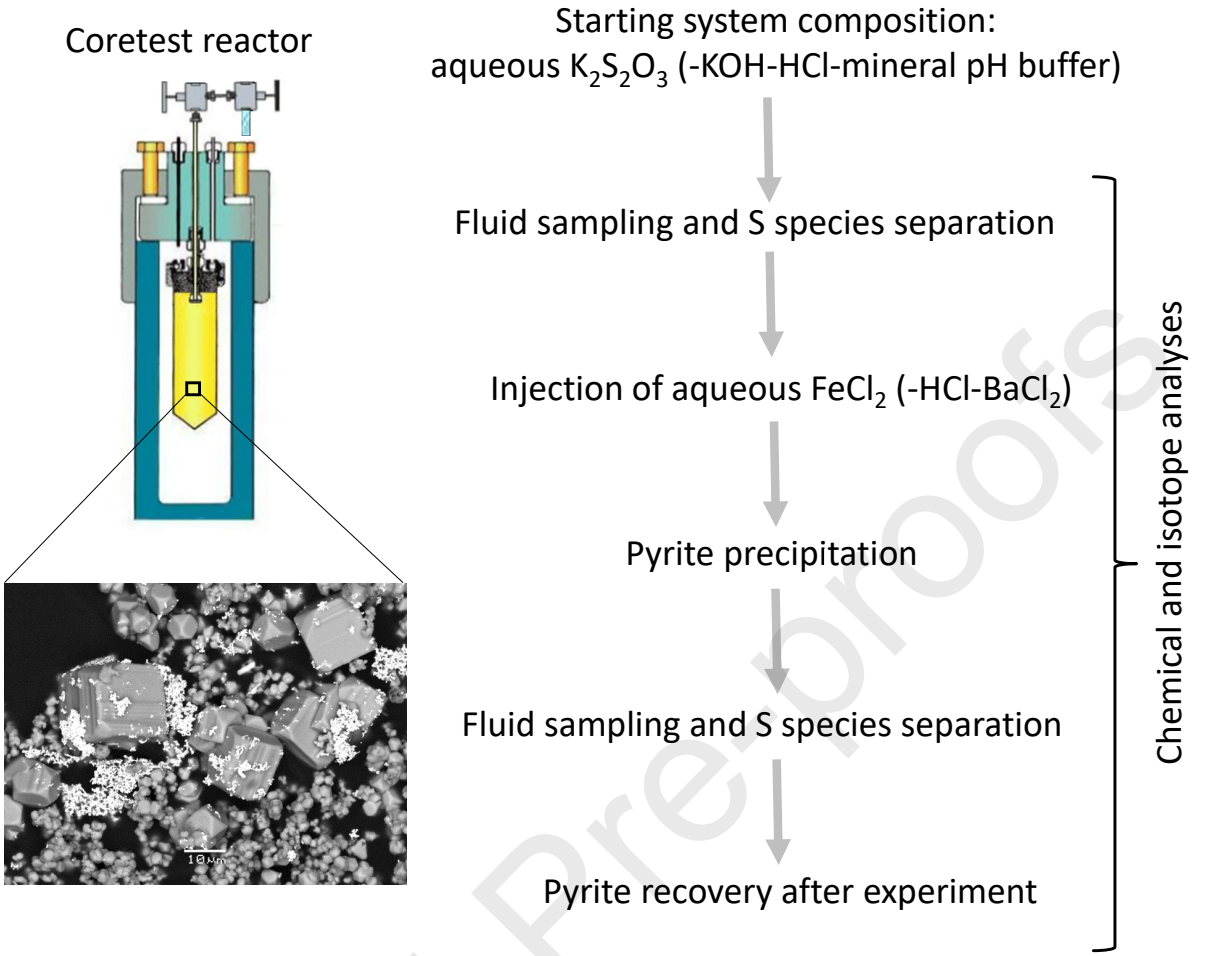

1335
1336
1337
1338 **Fig. 2**
1339

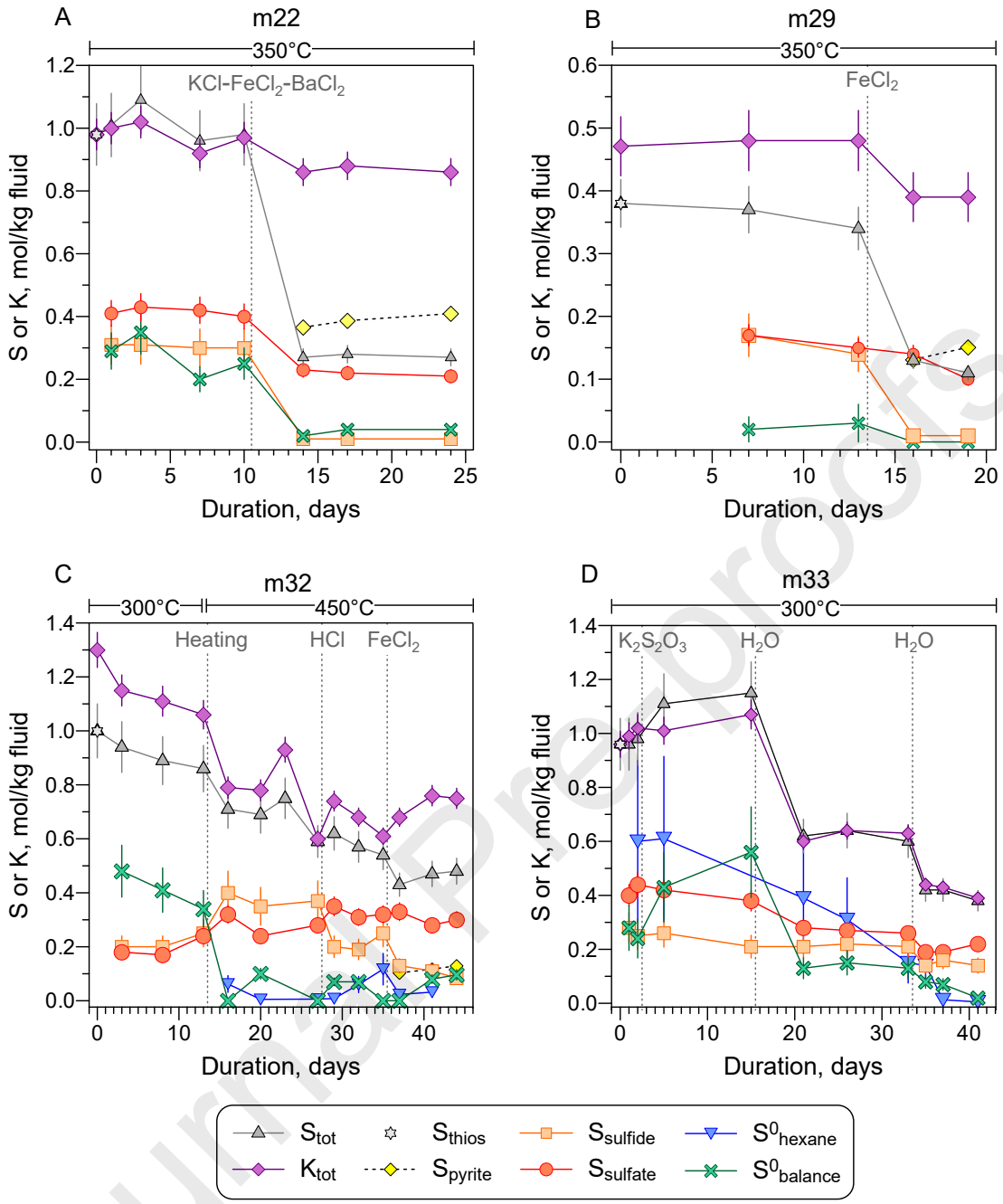

Fig. 3.

1346

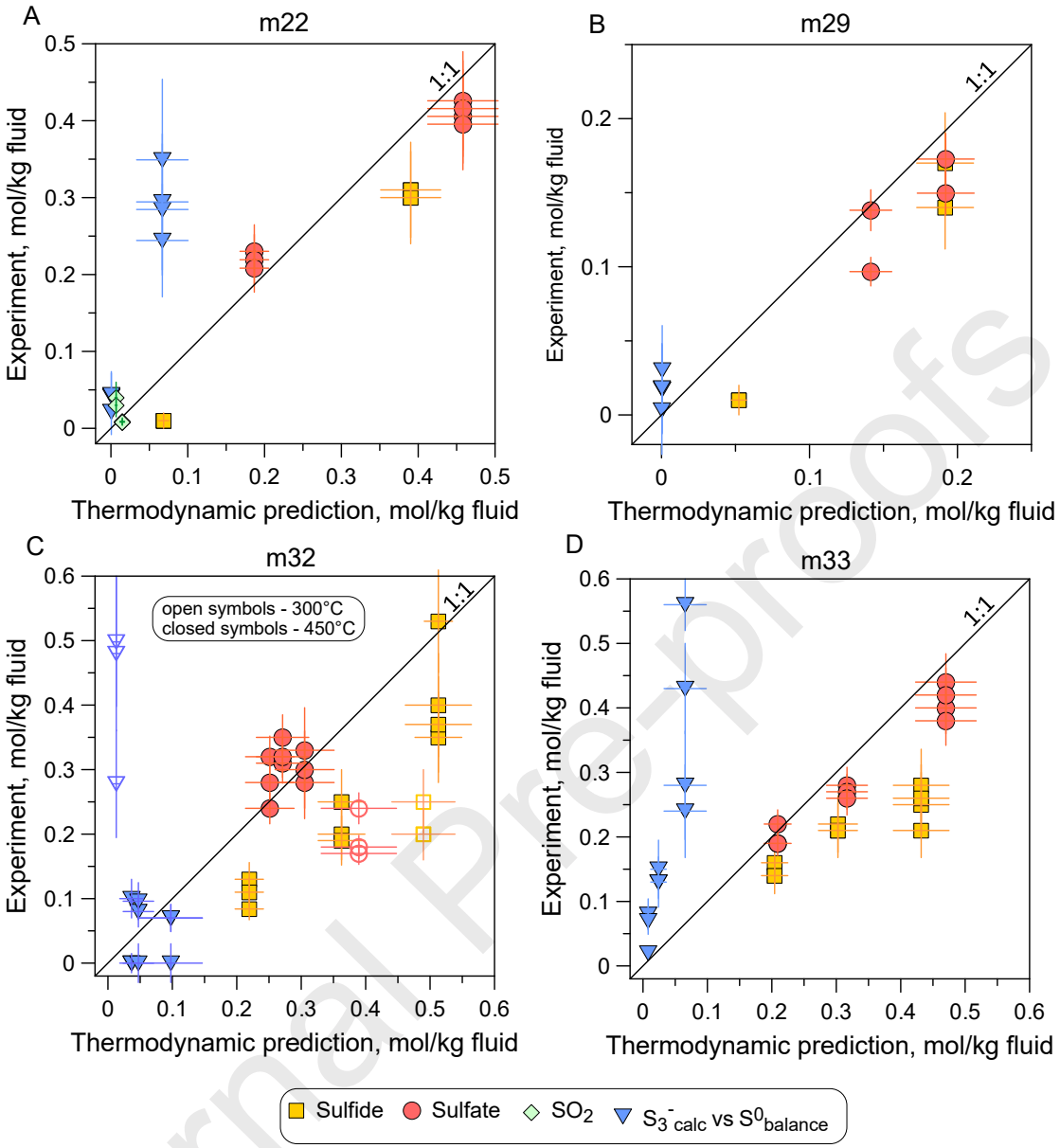

1347
1348
1349
1350 **Fig. 4.**
1351

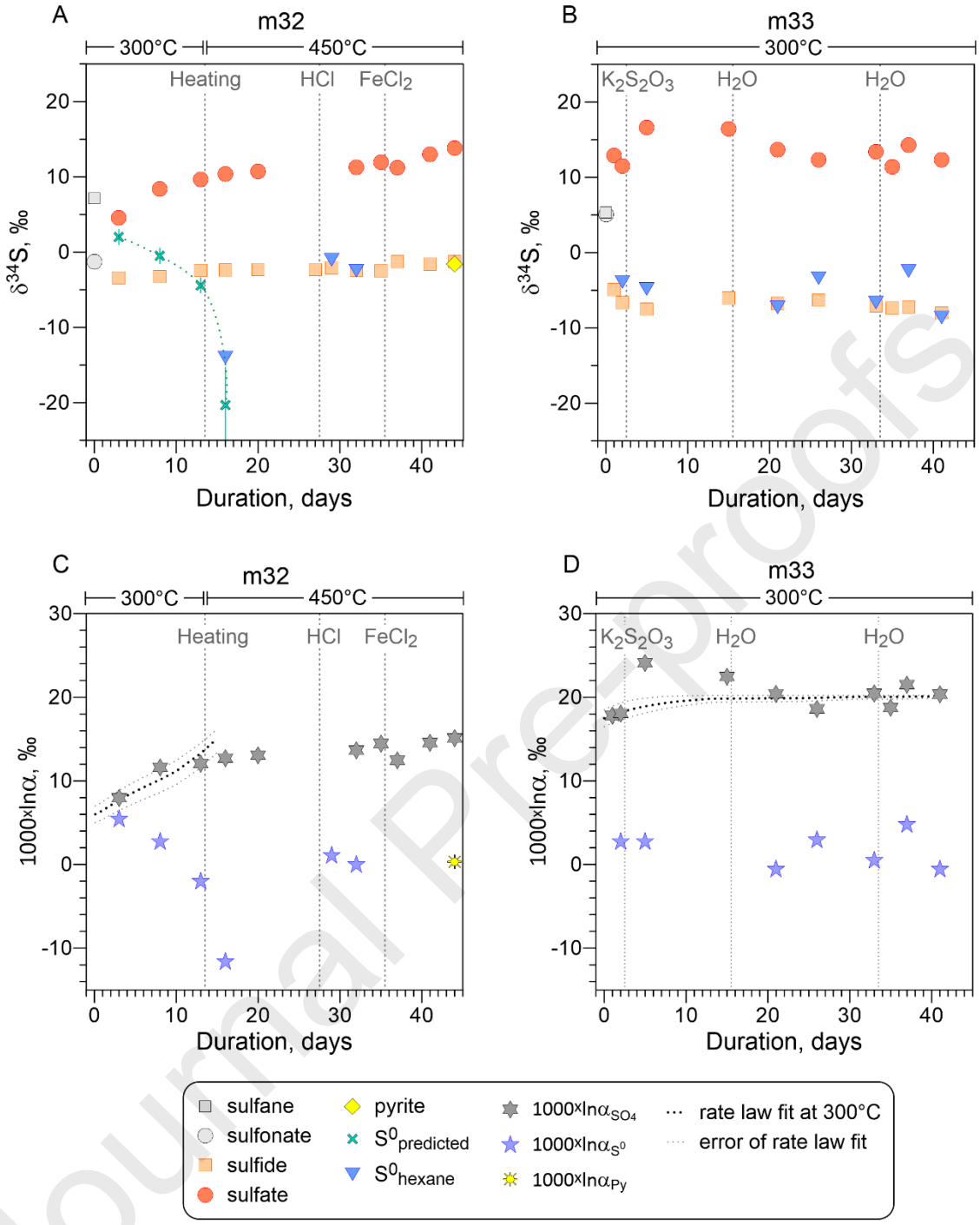

Fig. 5.

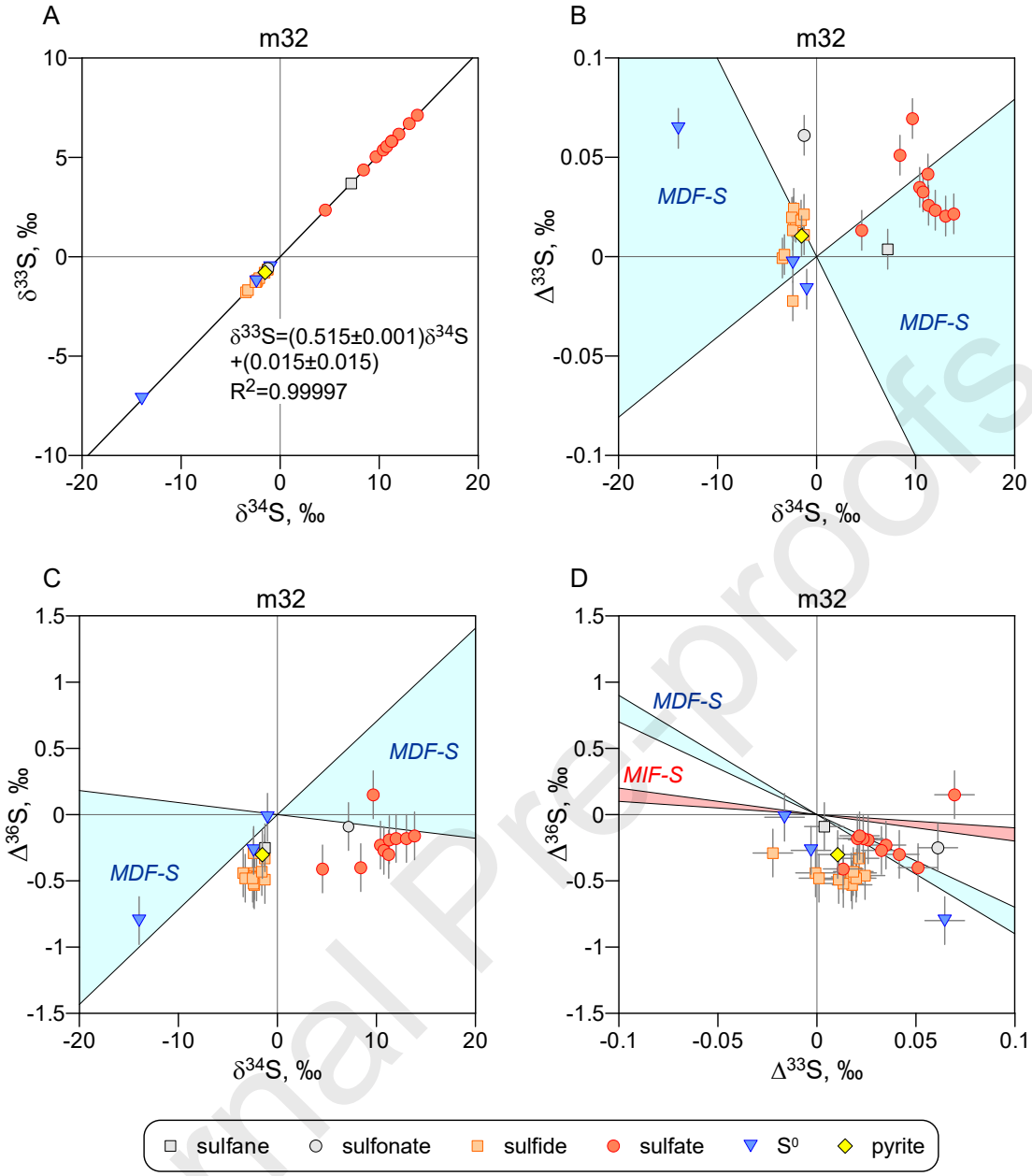

Fig. 6.

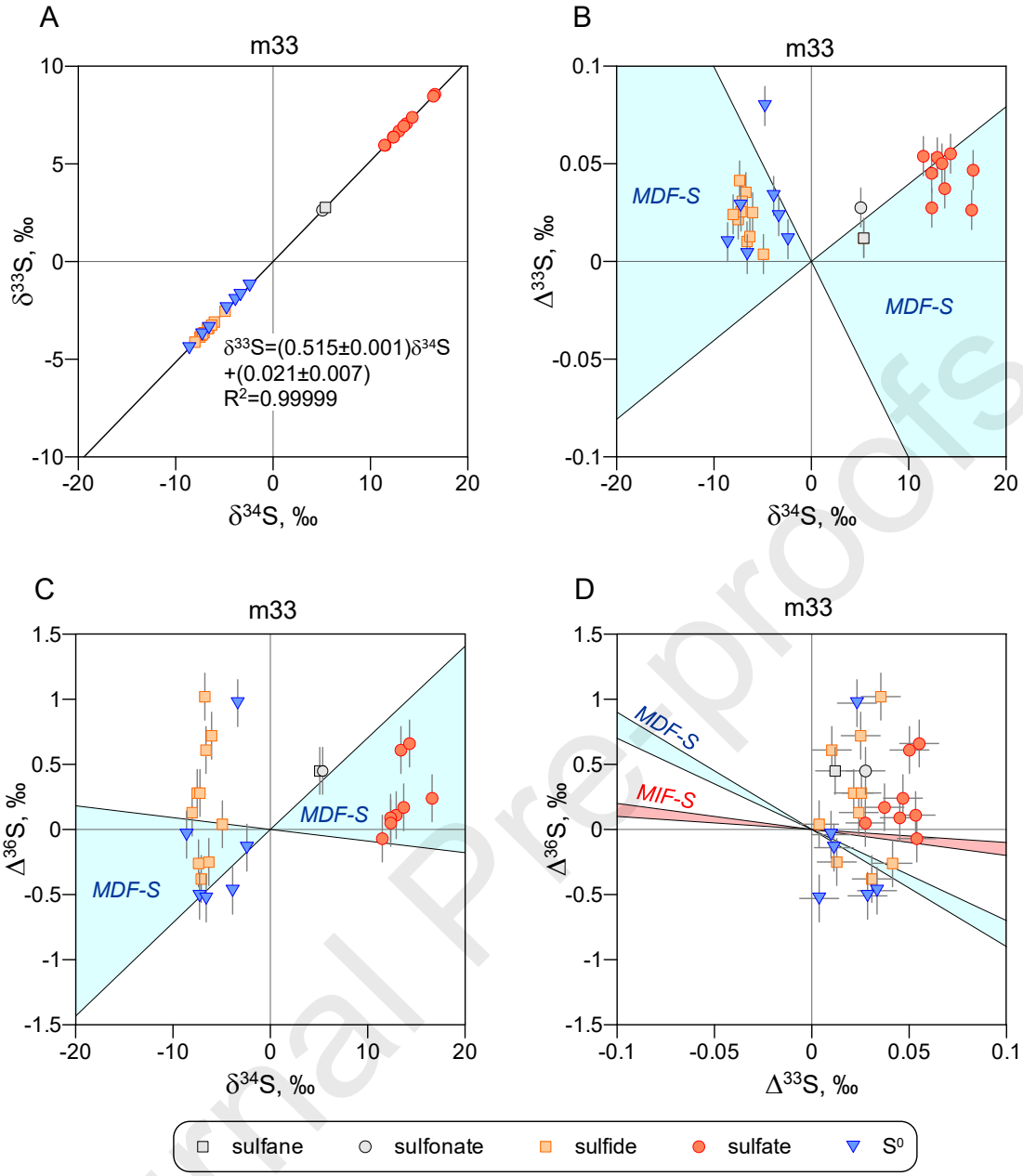

Fig. 7.

1367

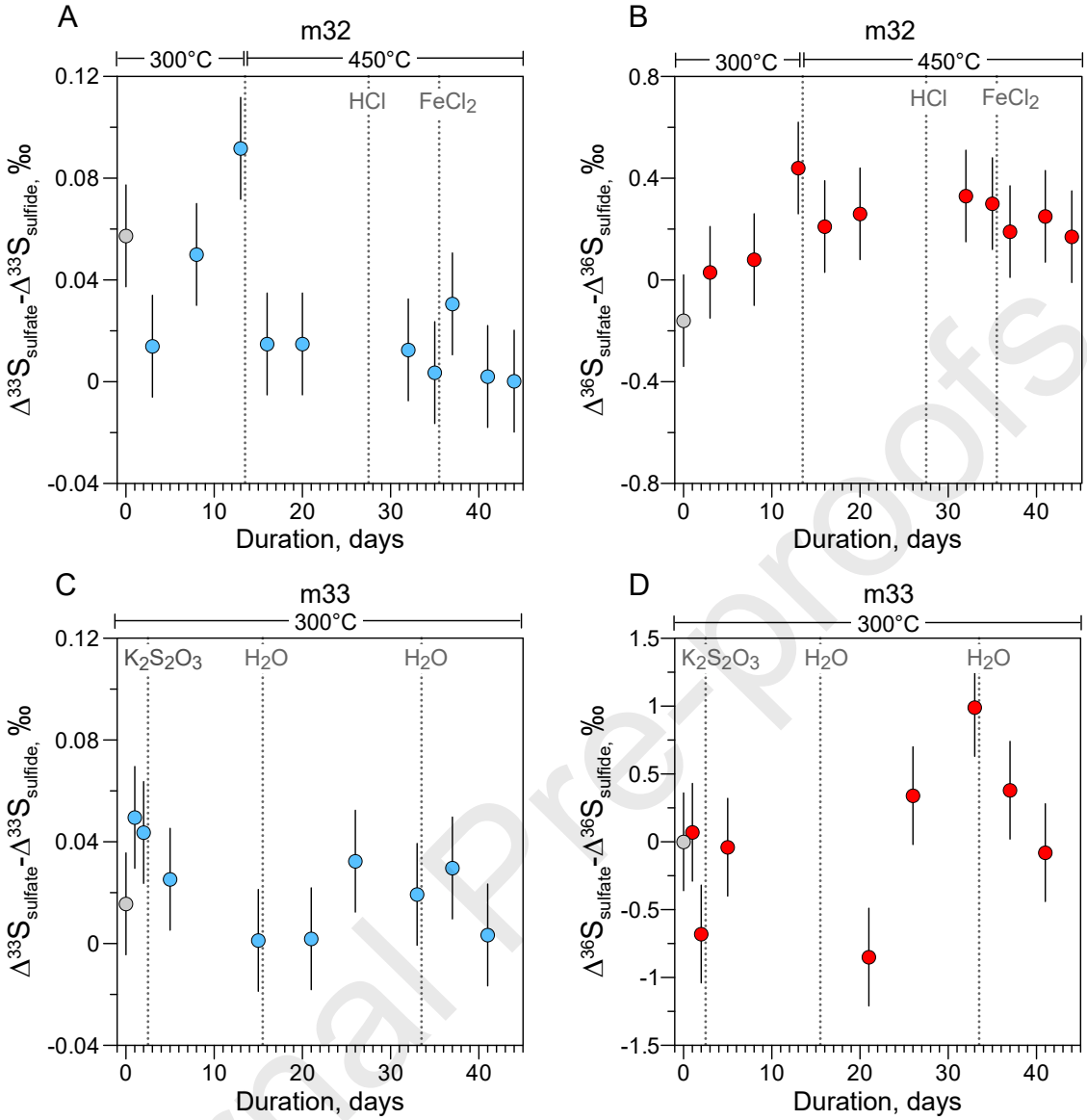

1368
1369
1370
1371 **Fig. 8.**
1372

1374

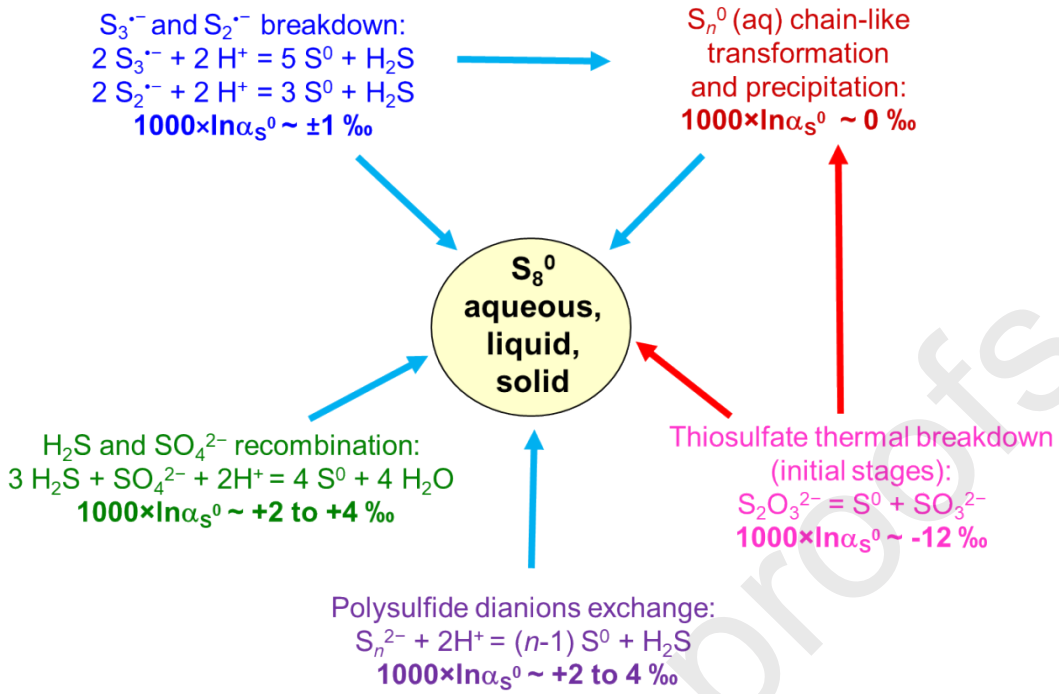

1375
1376
1377
1378 **Fig. 9.**